Efficient time-domain DG methods for wave propagation

Jesse Chan

[1]Department of Computational and Applied Mathematics
Rice University

ICES, UT Austin
April 6, 2017

Collaborators and contributors

- T. Warburton (Virginia Tech)
- Russell J. Hewett (TOTAL E&P Research and Technology USA)
- John Evans (U.C. Boulder)

Numerical simulation of wave propagation

Many procedures require **accurately** and **efficiently** solving hyperbolic partial differential equations (PDEs) in realistic settings.

- Seismic and medical imaging
- Engineering design
- Computational fluids

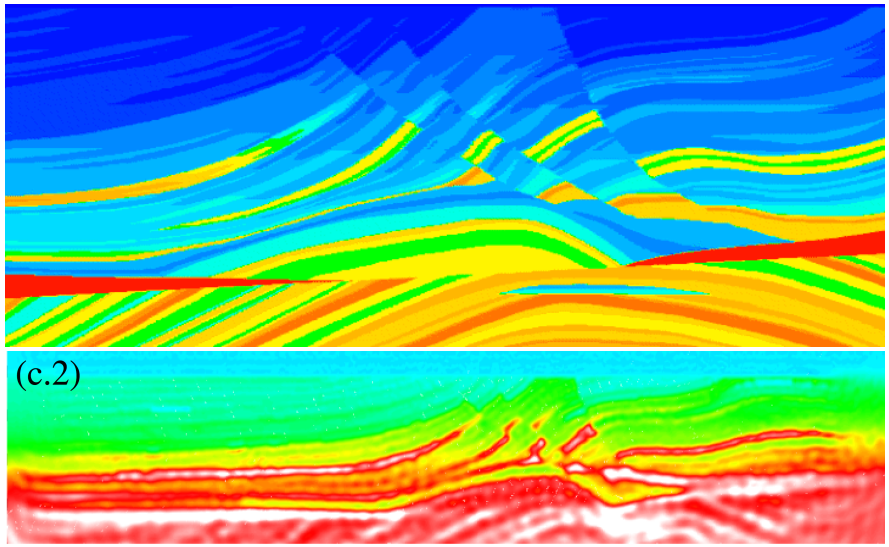

S. Scott Collis et al. Unstructured Discontinuous Galerkin for Seismic Inversion (Sandia).

Numerical simulation of wave propagation

Many procedures require **accurately** and **efficiently** solving hyperbolic partial differential equations (PDEs) in realistic settings.

- Seismic and medical imaging
- Engineering design
- Computational fluids

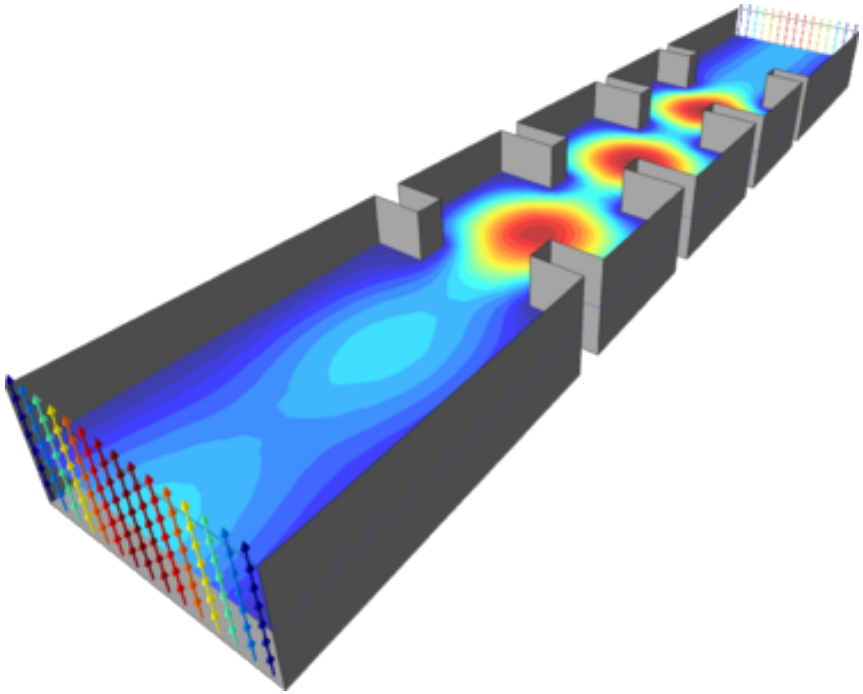

https://www.comsol.com/model/image/12737/big.png

Numerical simulation of wave propagation

Many procedures require **accurately** and **efficiently** solving hyperbolic partial differential equations (PDEs) in realistic settings.

- Seismic and medical imaging
- Engineering design
- Computational fluids

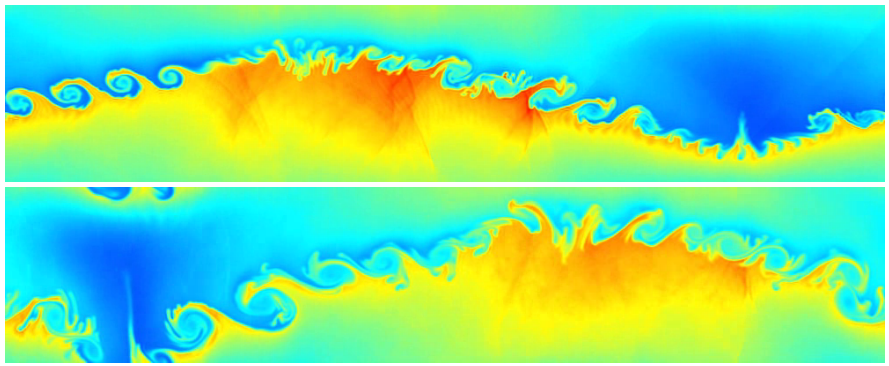

Per-Olof Persson, http://persson.berkeley.edu/research.html.

High order methods for wave problems

- Accurately represent acoustic and elastic waves.
- Superior performance vs low order methods for equivalent resolution.
- Low numerical dissipation and dispersion errors.
- Lower error per unknown.

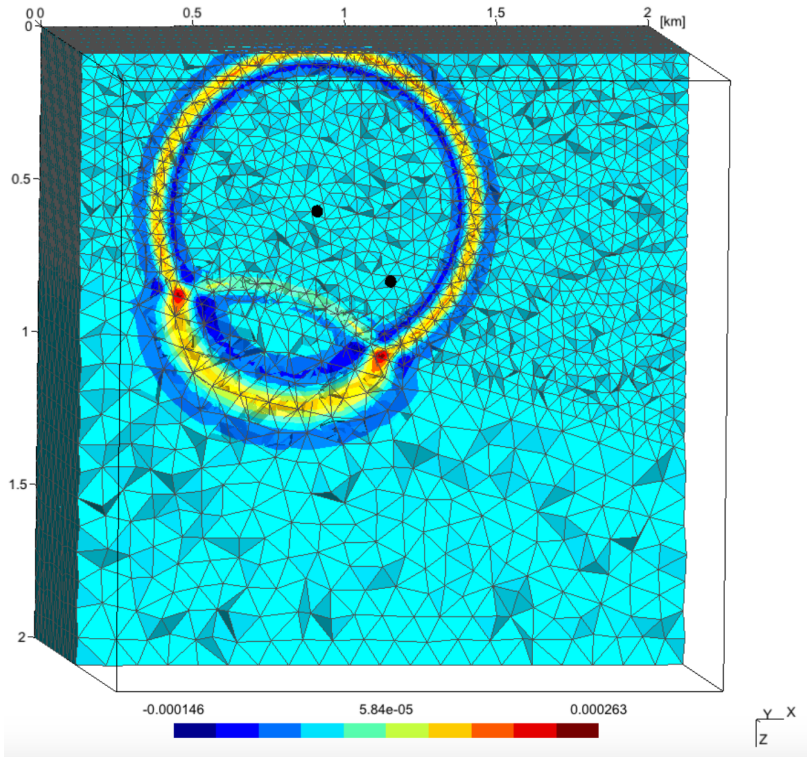

Figure courtesy of Axel Modave.

High order methods for wave problems

- Accurately represent acoustic and elastic waves.
- Superior performance vs low order methods for equivalent resolution.
- Low numerical dissipation and dispersion errors.
- Lower error per unknown.

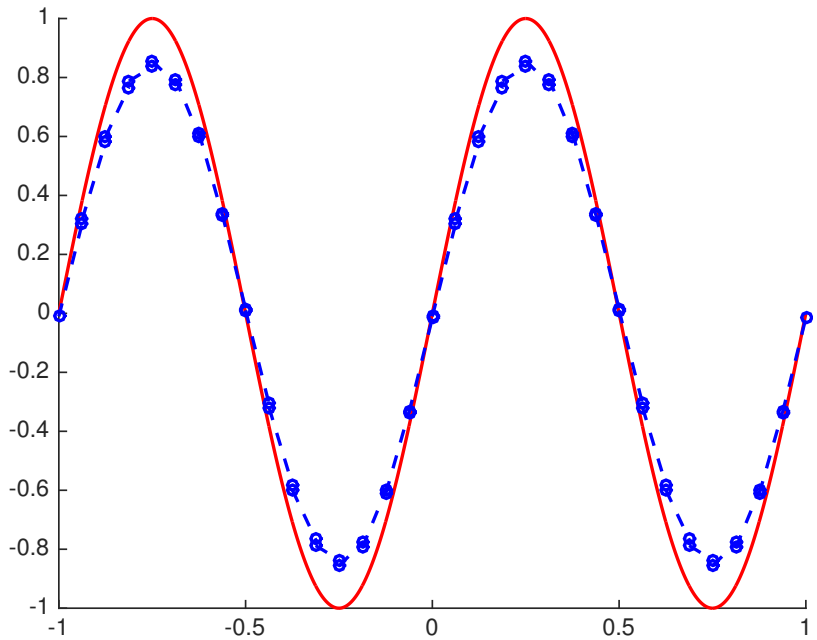

Fine linear approximation.

High order methods for wave problems

- Accurately represent acoustic and elastic waves.
- Superior performance vs low order methods for equivalent resolution.
- Low numerical dissipation and dispersion errors.
- Lower error per unknown.

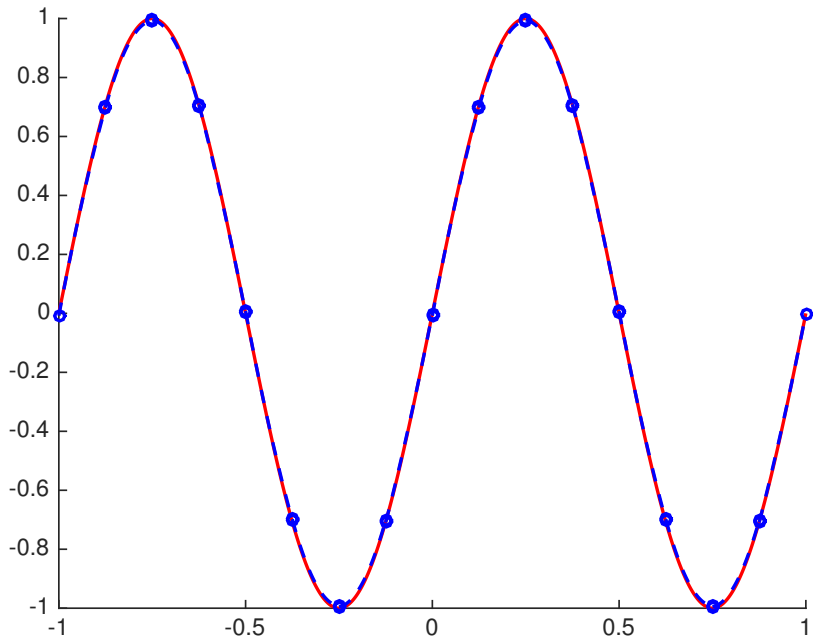

Coarse quadratic approximation.

High order methods for wave problems

- Accurately represent acoustic and elastic waves.
- Superior performance vs low order methods for equivalent resolution.
- Low numerical dissipation and dispersion errors.
- Lower error per unknown.

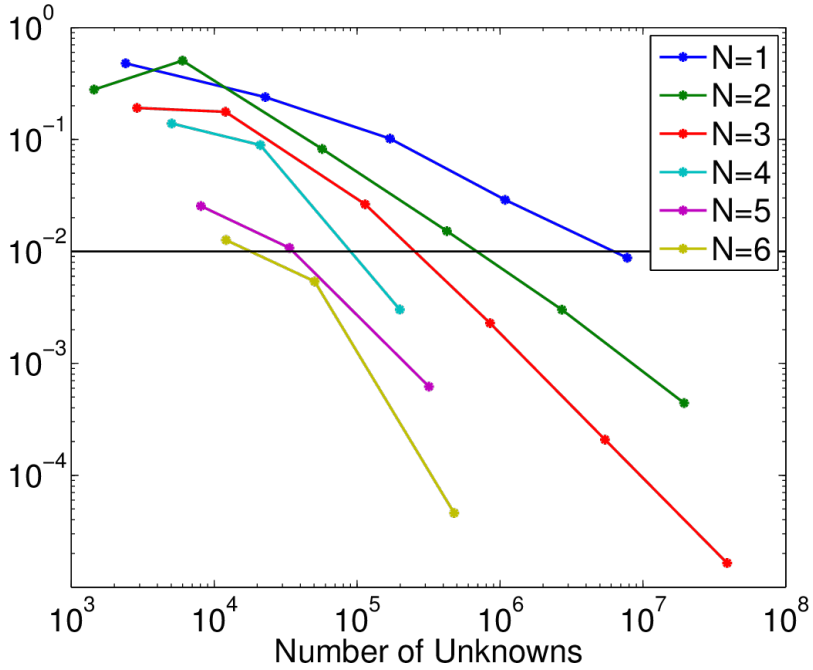

Max errors vs. dofs.

Discontinuous Galerkin methods

Discontinuous Galerkin (DG) methods:

- Piecewise polynomial approximation.
- Weak continuity across faces.

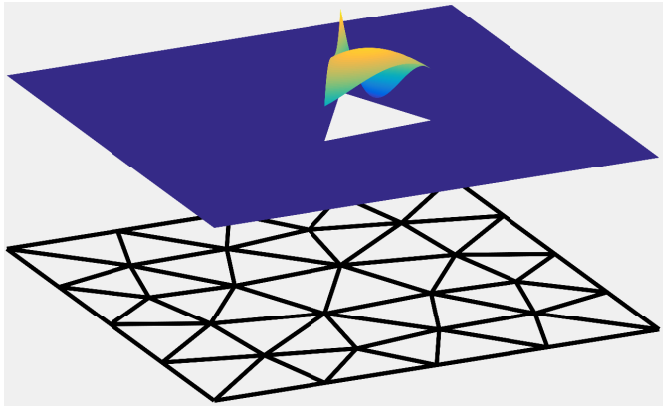

- Continuous PDE (example: advection)

$$\frac{\partial u}{\partial t} = \frac{\partial u}{\partial x}$$

- DG local weak form over D_k with numerical flux $\boldsymbol{f}^*$.

$$\int_{D_k} \frac{\partial u}{\partial t}\phi = \int_{D_k} \frac{\partial u}{\partial x}\phi + \int_{\partial D_k} \boldsymbol{n}\cdot(\boldsymbol{f}^* - \boldsymbol{f}(u))\,\phi, \qquad u, \phi \in V_h$$

Discontinuous Galerkin methods

Discontinuous Galerkin (DG) methods:

- Piecewise polynomial approximation.
- Weak continuity across faces.

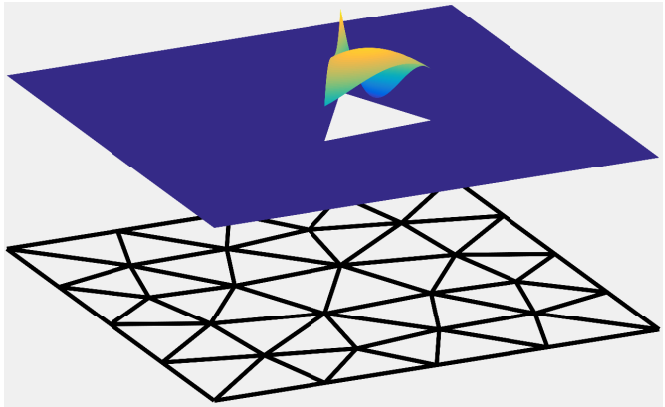

DG yields system of ODEs

$$\mathbf{M}_\Omega \frac{\mathrm{d}\mathbf{u}}{\mathrm{d}t} = \mathbf{A}\mathbf{u}.$$

DG mass matrix decouples across elements, inter-element coupling only through $\mathbf{A}$.

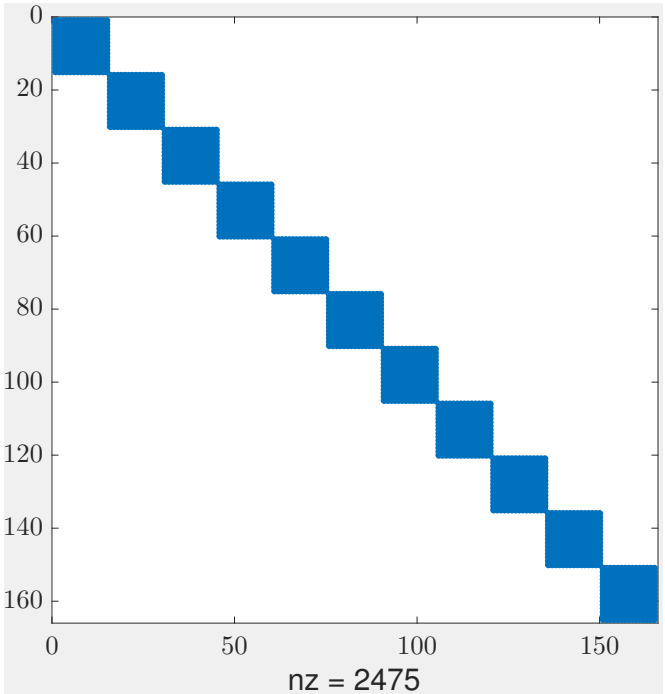

High order nodal discontinuous Galerkin methods

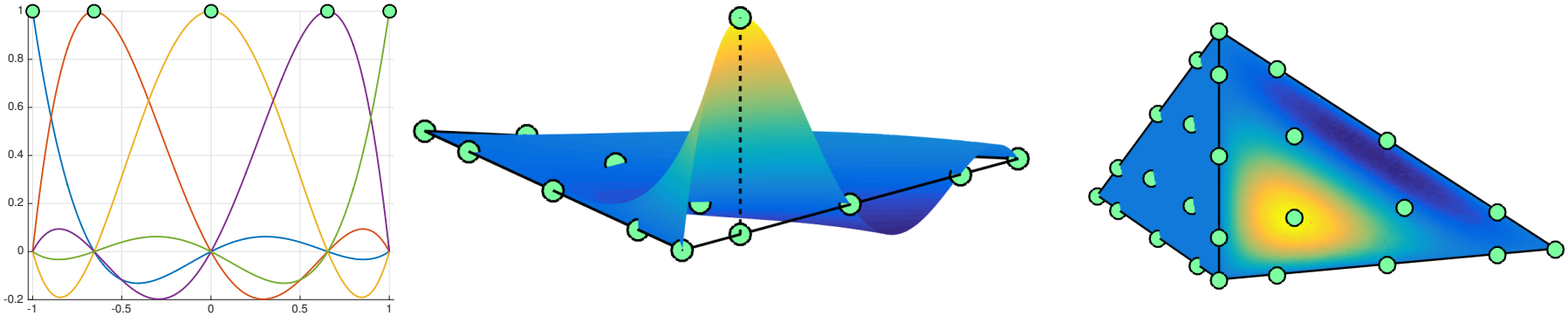

Lagrange (nodal) bases on a line, triangle, tetrahedron.

- Nodal bases defined implicitly through an orthogonal basis.
- Point locations optimized for interpolation and numerical stability.
- Assume **affine** tetrahedra, coefficients **constant** on each element.

Time-domain nodal DG methods

Given initial condition $u(\mathbf{x}, 0)$:

- Compute numerical flux at face nodes (non-local).
- Compute RHS of (local) ODE.
- Evolve (local) solution using explicit time integration (RK, AB, etc).

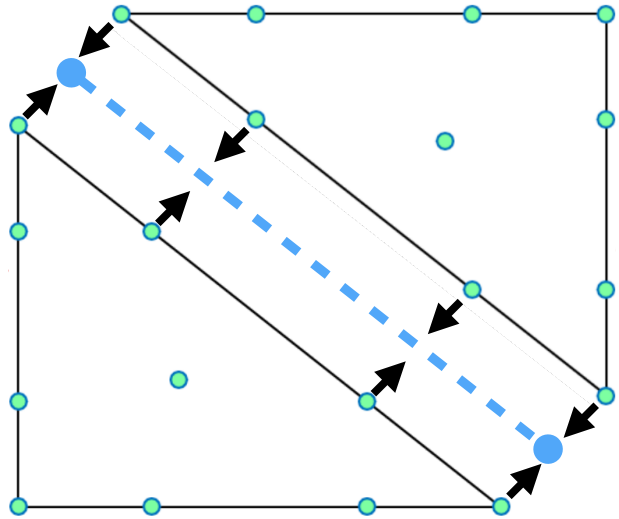

$$\frac{\mathrm{d}\mathbf{u}}{\mathrm{d}t} = \mathbf{D}_x\mathbf{u} + \sum_{\text{faces}} \mathbf{L}_f\,(\text{flux}), \qquad \mathbf{L}_f = \mathbf{M}^{-1}\mathbf{M}_f.$$

Parallelizable down to individual degrees of freedom!

Time-domain nodal DG methods

Given initial condition $u(\mathbf{x}, 0)$:

- Compute numerical flux at face nodes (non-local).
- Compute RHS of (local) ODE.
- Evolve (local) solution using explicit time integration (RK, AB, etc).

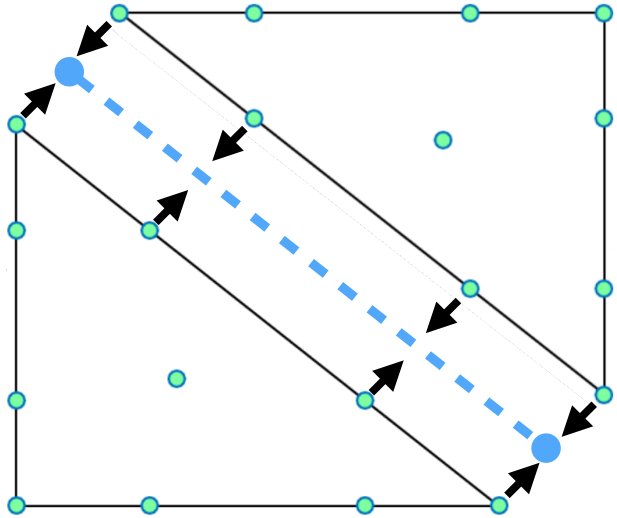

$$\frac{\mathrm{d}\mathbf{u}}{\mathrm{d}t} = \underbrace{\mathbf{D}_x\mathbf{u}}_{\text{Volume kernel}} + \underbrace{\sum_{\text{faces}} \mathbf{L}_f\,(\text{flux})}_{\text{Surface kernel}}, \qquad \mathbf{L}_f = \mathbf{M}^{-1}\mathbf{M}_f.$$

Parallelizable down to individual degrees of freedom!

Time-domain nodal DG methods

Given initial condition $u(\mathbf{x}, 0)$:

- Compute numerical flux at face nodes (non-local).
- Compute RHS of (local) ODE.
- Evolve (local) solution using explicit time integration (RK, AB, etc).

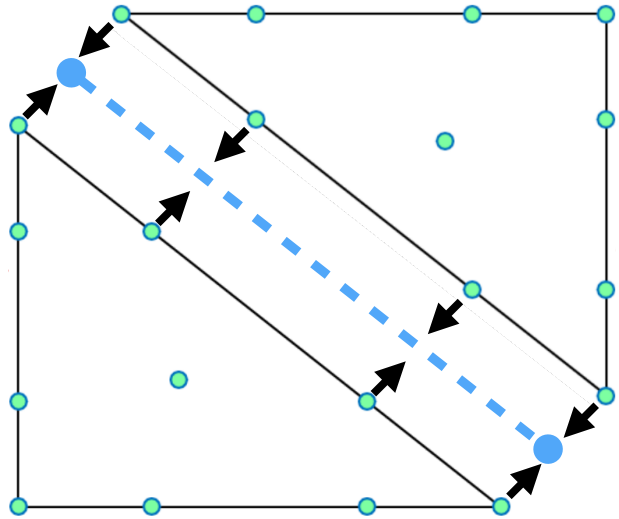

$$\underbrace{\frac{\mathrm{d}\mathbf{u}}{\mathrm{d}t}}_{\text{Update kernel}} = \underbrace{\mathbf{D}_x\mathbf{u}}_{\text{Volume kernel}} + \underbrace{\sum_{\text{faces}} \mathbf{L}_f\,(\text{flux})}_{\text{Surface kernel}}, \qquad \mathbf{L}_f = \mathbf{M}^{-1}\mathbf{M}_f.$$

Parallelizable down to individual degrees of freedom!

Time-domain nodal DG methods

Given initial condition $u(\mathbf{x}, 0)$:

- Compute numerical flux at face nodes (non-local).
- Compute RHS of (local) ODE.
- Evolve (local) solution using explicit time integration (RK, AB, etc).

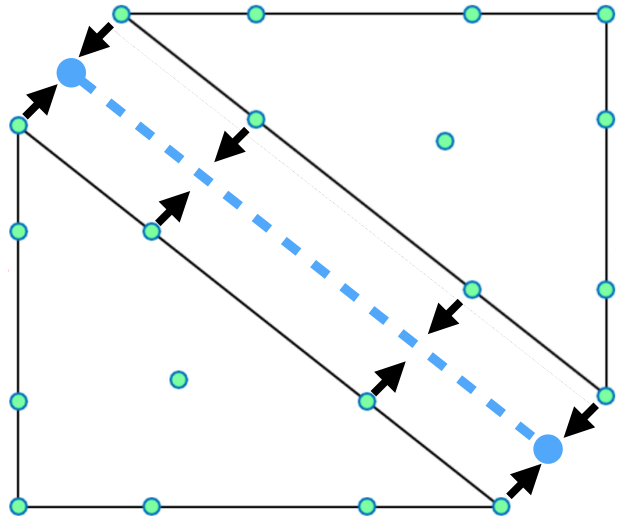

$$\underbrace{\frac{\mathrm{d}\mathbf{u}}{\mathrm{d}t}}_{\text{Update kernel}} = \underbrace{\mathbf{D}_x\mathbf{u}}_{\text{Volume kernel}} + \underbrace{\sum_{\text{faces}} \mathbf{L}_f\,(\text{flux})}_{\text{Surface kernel}}, \qquad \mathbf{L}_f = \mathbf{M}^{-1}\mathbf{M}_f.$$

Parallelizable down to individual degrees of freedom!

Computing with Graphics Processing Units (GPUs)

- Scalable but *expensive*: hours for 2D, **days** for 3D with ≈ 100 CPUs.
- Explicit methods: can replace a small cluster with single GPU.
- Highly energy efficient compared to traditional supercomputers.

  > *. . . to achieve a [next generation] supercomputer by simply [scaling up] . . . you'd need a good-size nuclear power plant next door. (Kogge 2011)*

- GPUs reflect broader many-core trends in computing.

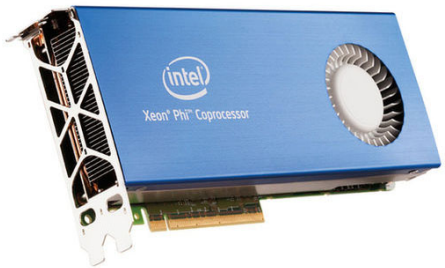

(a) Xeon Phi

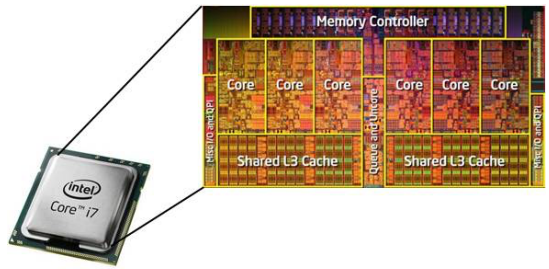

(b) Intel i7 CPU

DG maps well to many-core (GPU) architectures

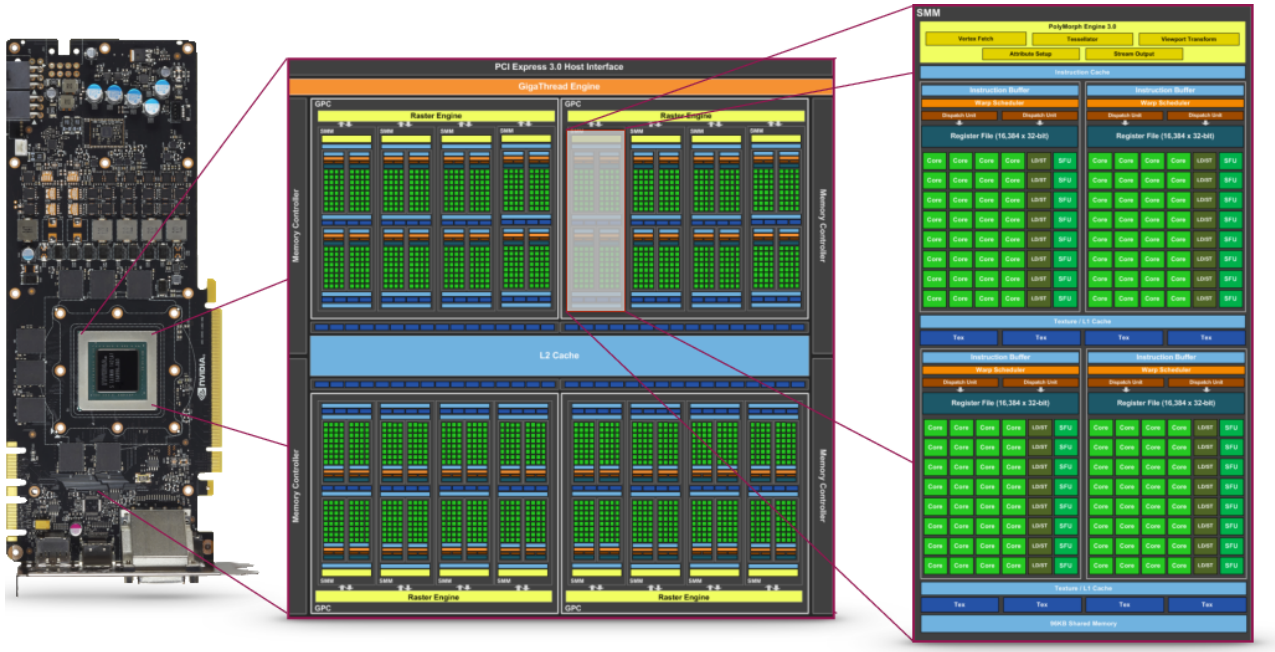

Figure: NVIDIA Maxwell GM204 GPU: 16 cores, 4 SIMD clusters of 32 units.

- Thousands of processing elements organized in synchronized groups.
- Stricter memory constraints (data transfer, limited storage), but ...
- For DG, reduces computational time from **days** to **hours**.

Klockner, Warburton, Bridge, Hesthaven 2009, Nodal discontinuous Galerkin methods on graphics processors.

DG maps well to many-core (GPU) architectures

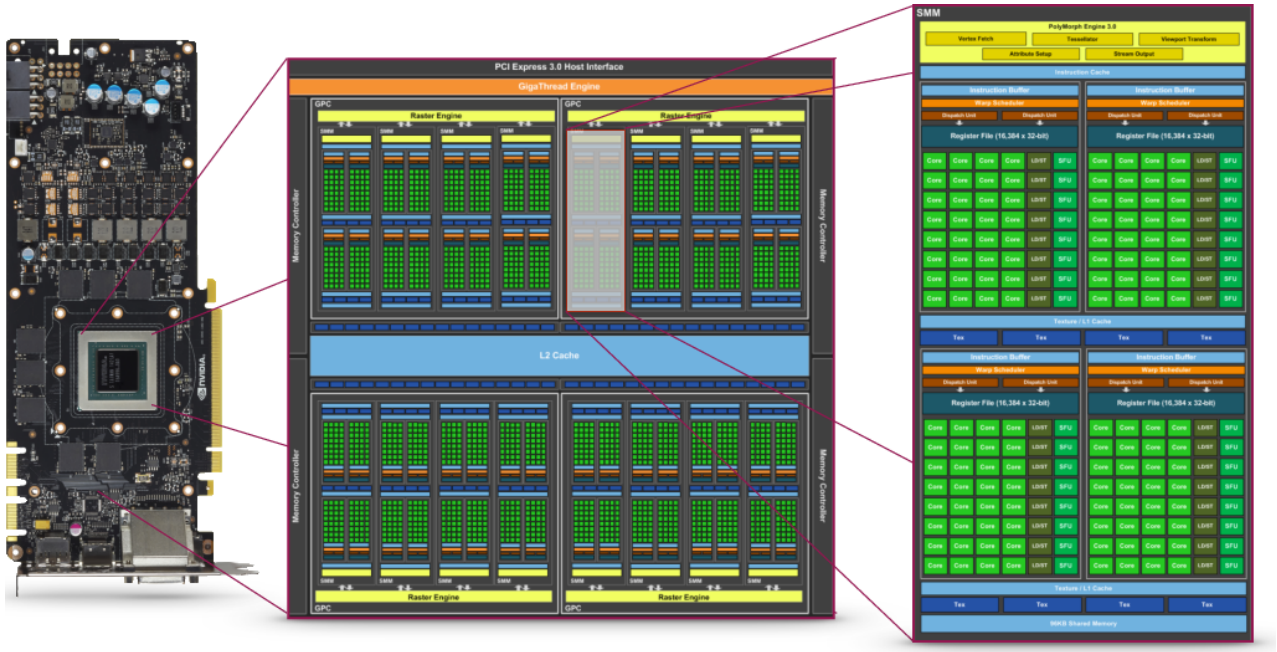

Figure: NVIDIA Maxwell GM204 GPU: 16 cores, 4 SIMD clusters of 32 units.

- Thousands of processing elements organized in synchronized groups.
- Stricter memory constraints (data transfer, limited storage), but ...
- For DG, reduces computational time from **days** to **hours**.

Klockner, Warburton, Bridge, Hesthaven 2009, Nodal discontinuous Galerkin methods on graphics processors.

DG maps well to many-core (GPU) architectures

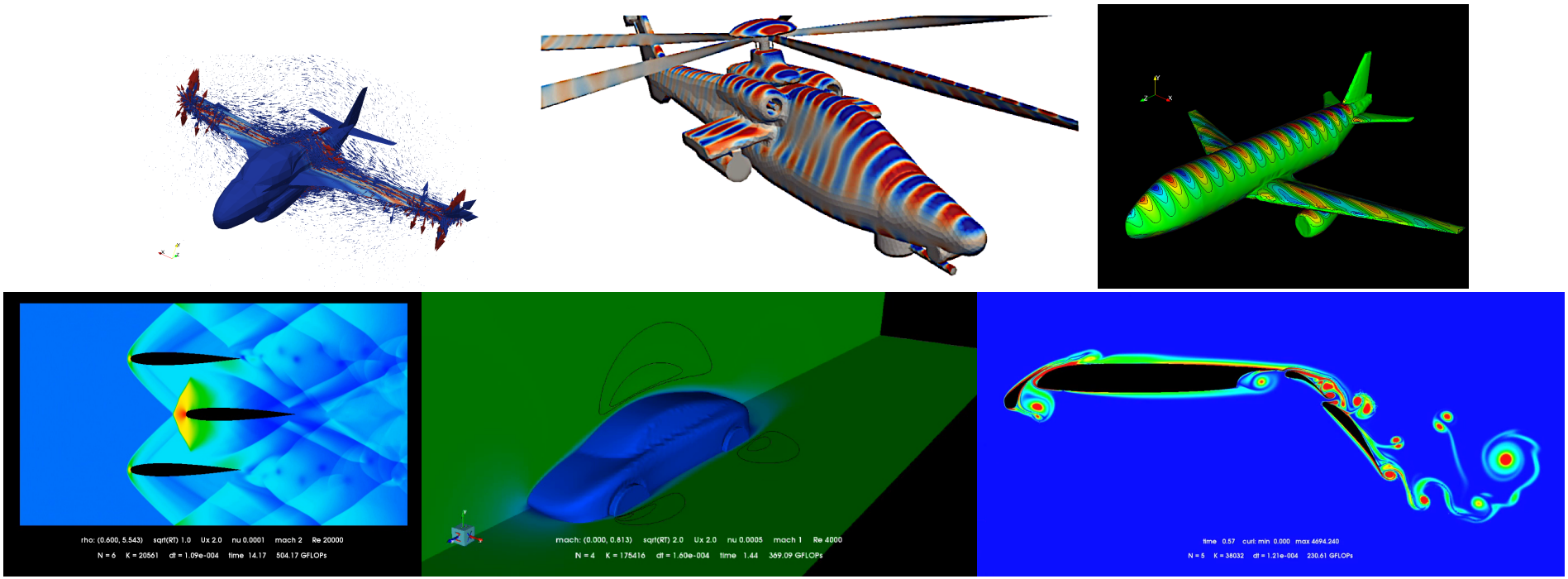

Figure: GPU-accelerated simulations of scattering and compressible flow.

- Thousands of processing elements organized in synchronized groups.
- Stricter memory constraints (data transfer, limited storage), but ...
- For DG, reduces computational time from **days** to **hours**.

Klockner, Warburton, Bridge, Hesthaven 2009, Nodal discontinuous Galerkin methods on graphics processors.

Outline: improving efficiency of time-domain DG

- Optimize existing DG methods on GPUs.
- Address simplifying assumptions (constant coefficients, affine tets).

1. GPU-accelerated DG methods
2. High order Bernstein-Bezier DG methods
3. Weight-adjusted DG: heterogeneous media
   - Curvilinear meshes
   - Elastic wave propagation

Outline: improving efficiency of time-domain DG

- Optimize existing DG methods on GPUs.
- Address simplifying assumptions (constant coefficients, affine tets).

1. GPU-accelerated DG methods
2. High order Bernstein-Bezier DG methods
3. Weight-adjusted DG: heterogeneous media
   - Curvilinear meshes
   - Elastic wave propagation

Computational costs at high orders of approximation

Problem: (tetrahedral) DG at high orders becomes **very** expensive!

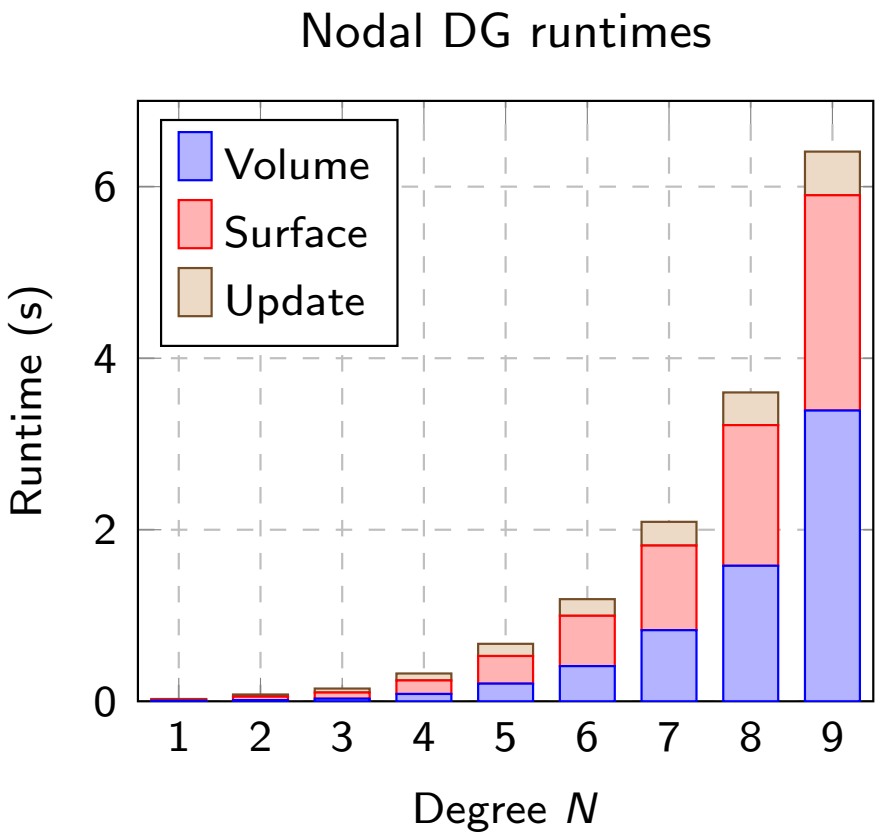

- Large **dense** matrices: $O(N^6)$ work per tet.
- Very high orders usually use tensor-product elements.
- $O(N^4)$ vs $O(N^6)$ cost, but less geometric flexibility.

DG runtimes for 50 timesteps, 98304 elements.

Spectral element methods

- Tensor product elements, Gauss-Legendre-Lobatto nodal basis.
- $O(N^{d+1})$ vs $O(N^{2d})$ work per element (computing derivatives).
- Hexahedral mesh generation more difficult.

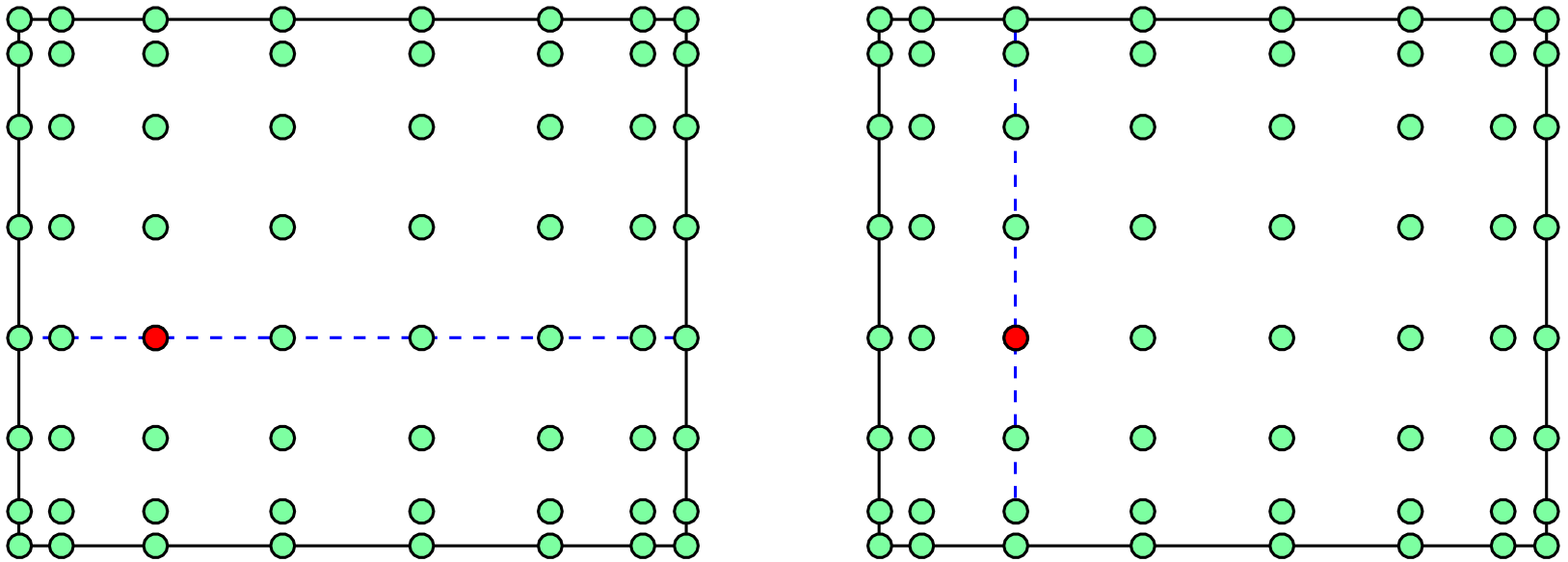

Figure: Spectral element stencils for $N = 7$ (orders $N > 10$ not uncommon!).

Fischer, Ronquist 1994. Spectral element methods for large scale parallel Navier-Stokes calculations.

Shepherd and Johnson 2008. Hexahedral mesh generation constraints.

High order nodal DG on tetrahedral meshes

$$\frac{\mathrm{d}\mathbf{u}}{\mathrm{d}t} = \mathbf{D}_x\mathbf{u} + \sum_{\text{faces}} \mathbf{L}_f\,(\text{flux})\,, \quad \mathbf{L}_f = \mathbf{M}^{-1}\mathbf{M}_f.$$

- Nodal bases: reduce the cost of computing numerical fluxes.
- No special structure in nodal derivative/lift matrices.
- $O(N^3)$ unknowns in 3D; $O(N^6)$ costs for applying **dense** matrices.

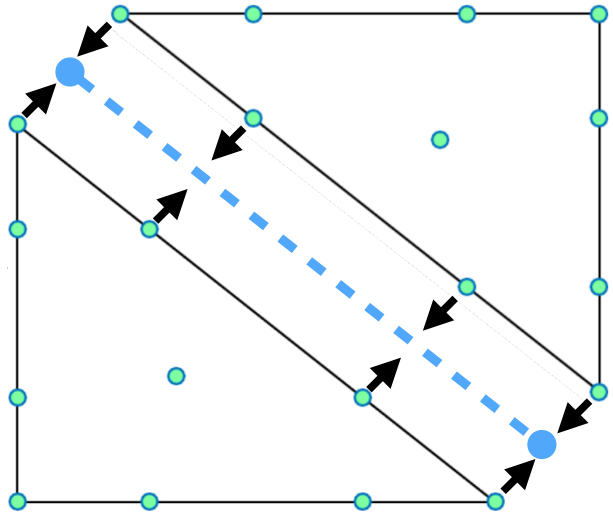

Derivative and lift matrices depend on the basis:
can we choose one that is efficient (and numerically stable)?

Bernstein-Bezier bases for finite element methods

- Geometry, graphics, Computer Aided Design (CAD).

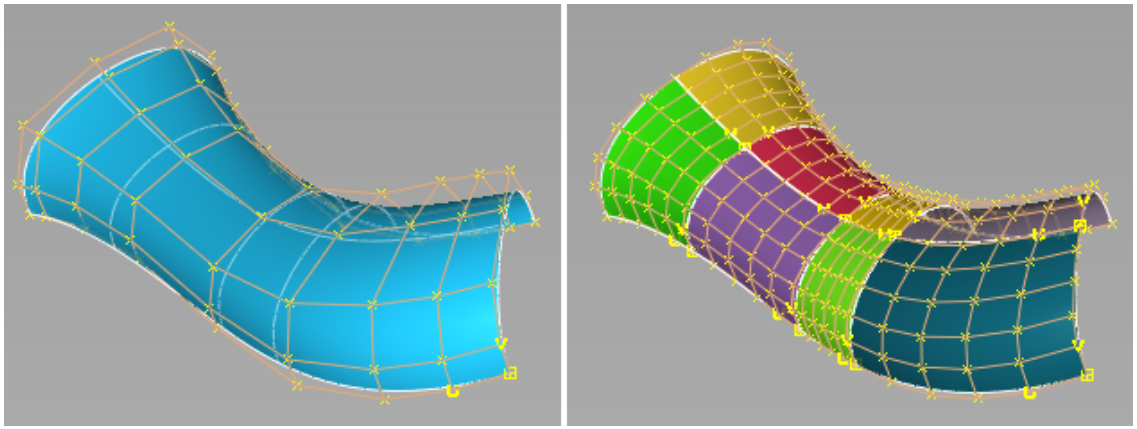

- Recent developments: optimal complexity algorithms for quadrature-based integration, assembly of finite element matrices.
- Is Bernstein-Bezier useful for quadrature-free DG methods?

Split multi-span NURBS surfaces into Bezier patches, https://knowledge.autodesk.com

Ainsworth et al. 2011. Bernstein-Bezier finite elements of arbitrary order and optimal assembly procedures.

Kirby 2011. Fast simplicial finite element algorithms using Bernstein polynomials.

Bernstein-Bezier polynomial bases on simplices

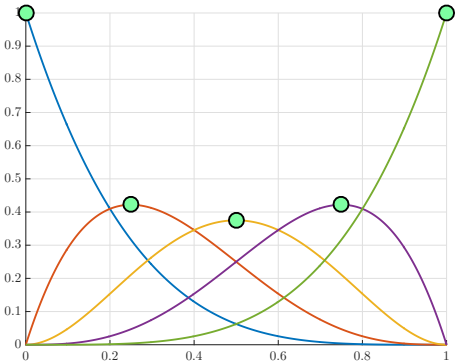

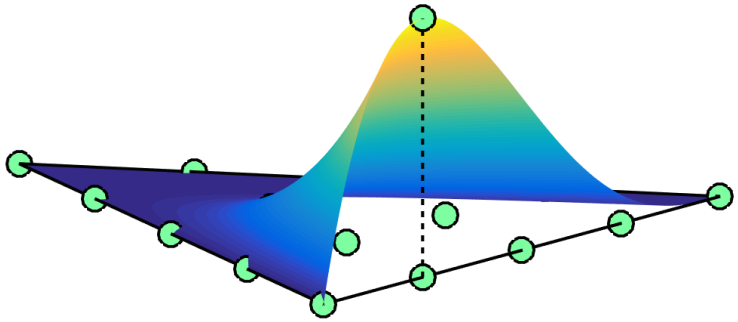

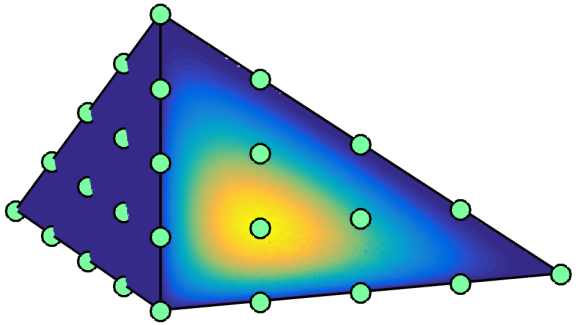

Each function attains its maximum at an equispaced lattice point of a d-simplex.

- Simple expression in 1D

$$B_i^N(x) = x^i(1-x)^{N-i}, \qquad 0 \le x \le 1.$$

- Barycentric monomials on a d-simplex. For a tetrahedron,

$$B_{ijkl}^N(\lambda_0,\lambda_1,\lambda_2,\lambda_3), = \frac{N!}{i!j!k!l!}\lambda_0^i\lambda_1^j\lambda_2^k\lambda_3^l, \quad i+j+k+l=N.$$

- Similar structure to nodal basis (vertex, edge, face, interior functions).

Bernstein-Bezier derivatives and degree elevation in 1D

- Simple differentiation of Bernstein polynomials

$$\frac{\partial B_i^N(x)}{\partial x} = N\left(B_{i-1}^{N-1}(x) - B_i^{N-1}(x)\right).$$

- Simple degree elevation of Bernstein polynomials

$$B_i^{N-1}(x) = \left(\frac{N-i}{N}\right) B_i^N(x) - \left(\frac{i+1}{N}\right) B_{i+1}^N(x).$$

- Combine to get expansion of Bernstein derivatives

$$\frac{\partial B_i^N(x)}{\partial x} = a_i^N B_{i-1}^N(x) + b_i^N B_i^N(x) - c_i^N B_{i+1}^N(x).$$

Implies 1D derivative matrix $\mathbf{D}_x$ is sparse (tridiagonal).

Bernstein-Bezier derivative and degree elevation in 3D

- Bernstein-Bezier barycentric differentiation matrices very sparse.
- Degree elevation matrices $\mathbf{E}_{N-i}^{N}$ are sparse (for consecutive degrees).
- Higher degree elevation $\rightarrow$ product of matrices $\mathbf{E}_{N-2}^{N} = \mathbf{E}_{N-1}^{N}\mathbf{E}_{N-2}^{N-1}$.

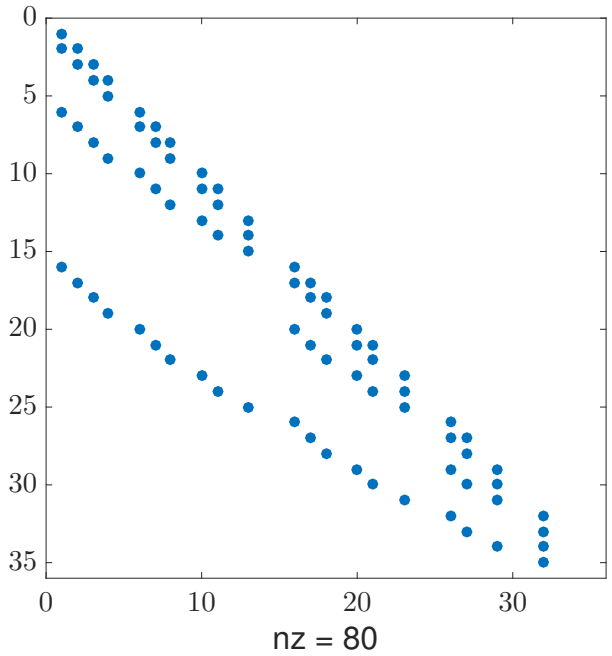

(a) Derivative matrix w.r.t. first barycentric coordinate.

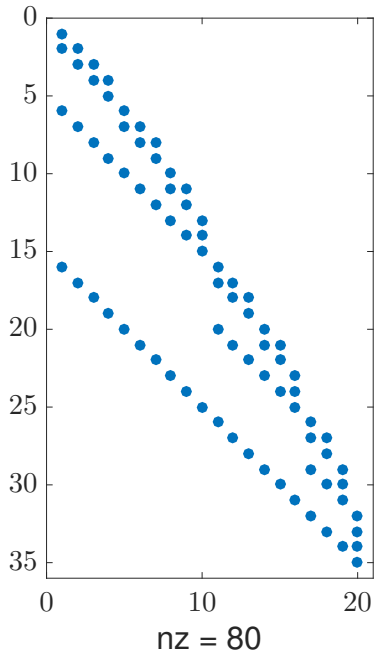

(b) Deg. elevation matrix $\mathbf{E}_{N-1}^{N}$

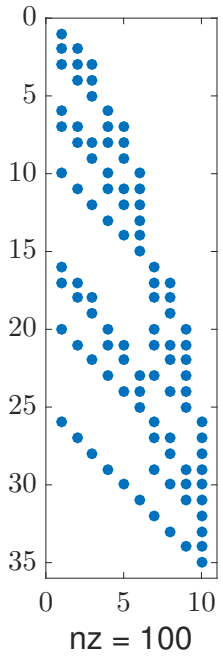

(c) $\mathbf{E}_{N-2}^{N}$

Stencils for Bernstein-Bezier derivative matrices

- Stencil sizes at most $(d+1)$ in d dimensions.
- Compute derivatives w.r.t. barycentric coordinates.
- Stencil values are identical for each barycentric coordinate.

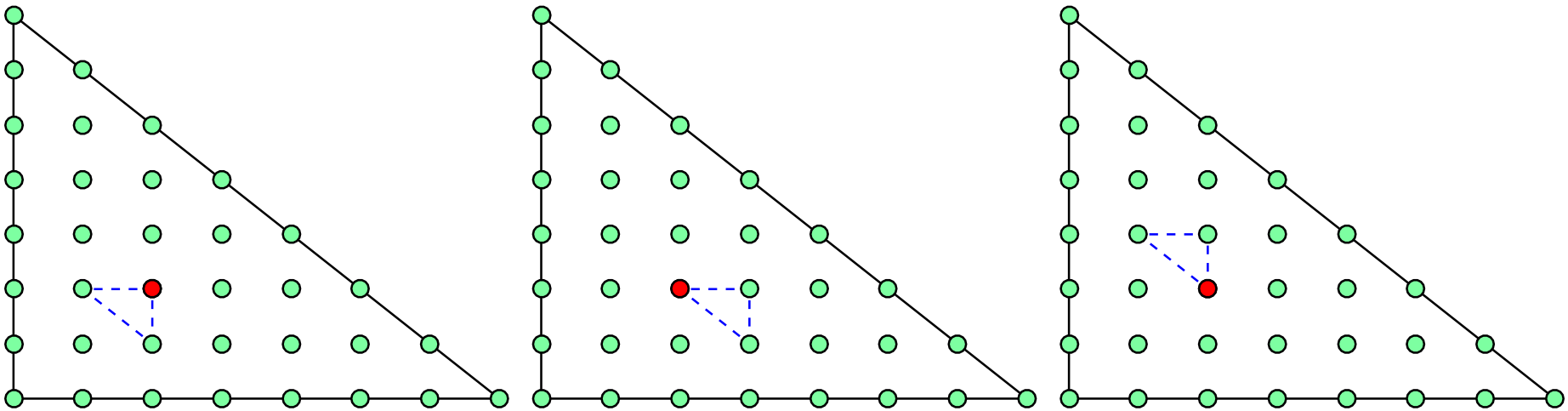

(d) Stencil for $\boldsymbol{D}_{\lambda_0}$ (e) Stencil for $\boldsymbol{D}_{\lambda_1}$ (f) Stencil for $\boldsymbol{D}_{\lambda_2}$

Figure: Bernstein-Bezier stencils for a single node (in red) $N = 7$.

Factorization of the Bernstein lift operator

The Bernstein-Bezier lift matrix $\mathbf{L}$ admits a factorization of the form

$$\mathbf{L} = \mathbf{E}_L \begin{pmatrix} \mathbf{L}_0 & & & \\ & \mathbf{L}_0 & & \\ & & \mathbf{L}_0 & \\ & & & \mathbf{L}_0 \end{pmatrix}.$$

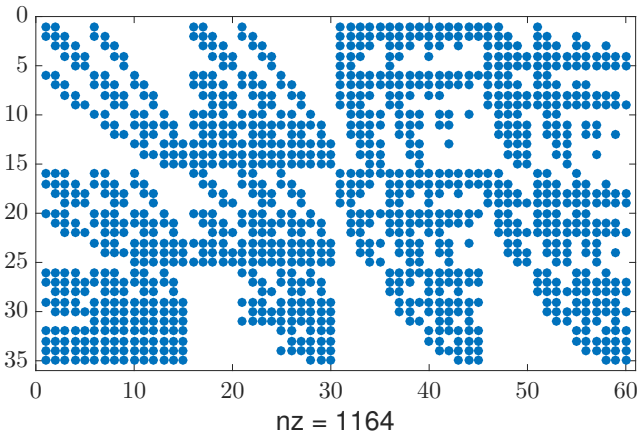

(a) Lift matrix $\mathbf{L}$

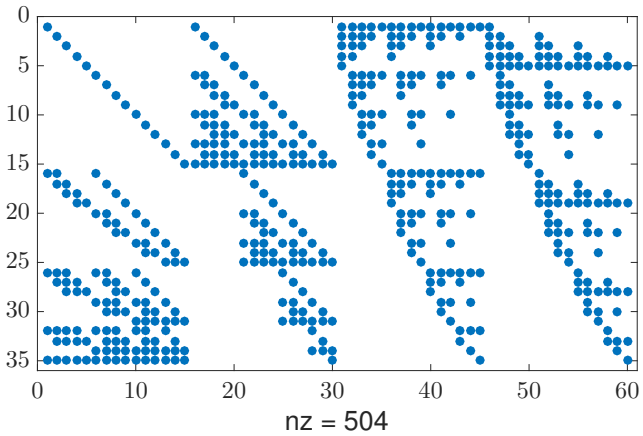

(b) Lift reduction $\mathbf{E}_L$

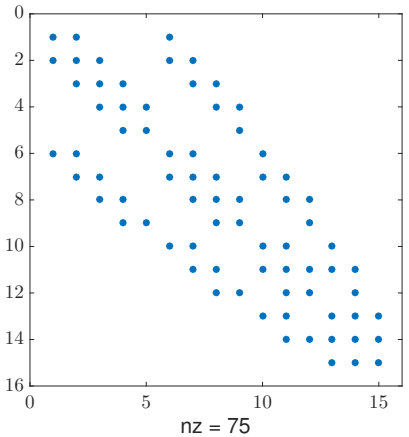

(c) $\mathbf{L}_0$

Chan, Warburton 2015. GPU-accelerated Bernstein-Bezier DG methods for wave problems.

Factorization of the Bernstein lift operator

The Bernstein-Bezier lift matrix $\mathbf{L}$ admits a factorization of the form

$$\mathbf{L} = \mathbf{E}_L \begin{pmatrix} \mathbf{L}_0 & & & \\ & \mathbf{L}_0 & & \\ & & \mathbf{L}_0 & \\ & & & \mathbf{L}_0 \end{pmatrix}.$$

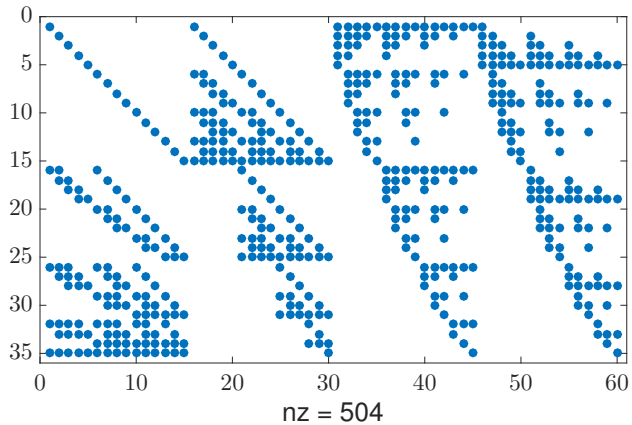

$\mathbf{E}_L = \left[\begin{array}{c|c|c|c} \mathbf{E}_L^1 & \ldots & \mathbf{E}_L^4 \end{array} \right]$ (4 faces).

$$\mathbf{E}_L^1 = \begin{bmatrix} \mathbf{I} \\ \ell_1 \left(\mathbf{E}_{N-1}^N\right)^T \\ \vdots \\ \ell_N \left(\mathbf{E}_0^N\right)^T \end{bmatrix}.$$

2D degree reduction matrices $\left(\mathbf{E}_i^N\right)^T$.

Chan, Warburton 2015. GPU-accelerated Bernstein-Bezier DG methods for wave problems.

Bernstein-Bezier lift matrix: optimal complexity application

- $\boldsymbol{L}$ "lifts" numerical fluxes from faces to volume.
- Apply $\boldsymbol{L}_0$ to face flux, extend to each "layer" of the simplex.

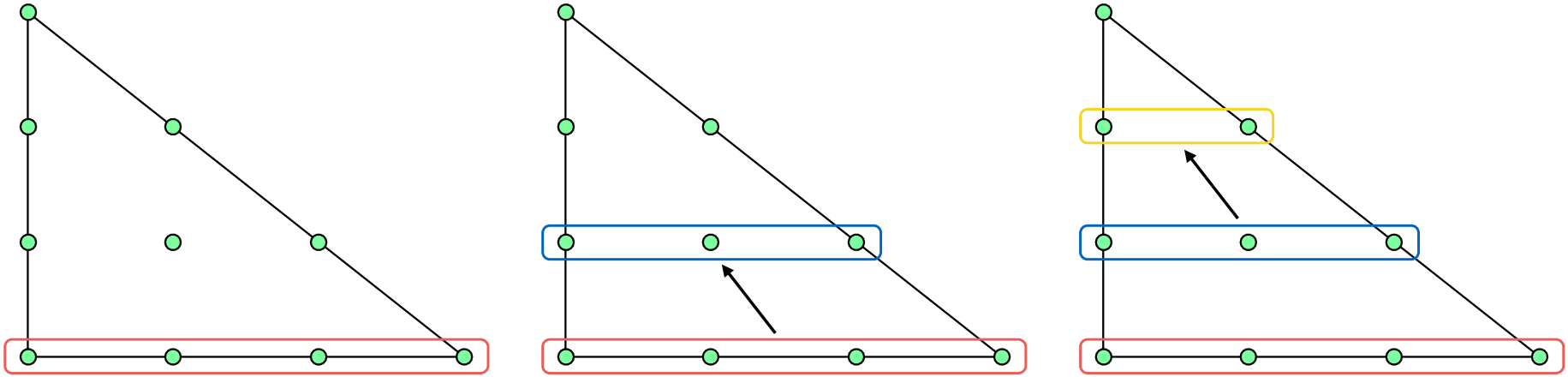

(a) Apply $\boldsymbol{L}_0$ to flux to compute face output

(b) Degree reduce face nodes to compute first layer

(c) Degree reduce first layer to compute second layer

Figure: An $O(N^d)$ storage/complexity approach to applying the lift matrix.

For $N < 6$, currently more efficient to treat $\boldsymbol{E}_L$ as a sparse matrix — irregular data accesses with optimal $O(N^d)$ approach.

Numerical stability of Bernstein-Bezier DG

- Conditioning of derivative, lift matrices comparable to nodal basis.

$$\kappa(\mathbf{A}) = \frac{\sigma_1}{\sigma_r}$$

- Comparable long-time growth of (single precision) numerical error.

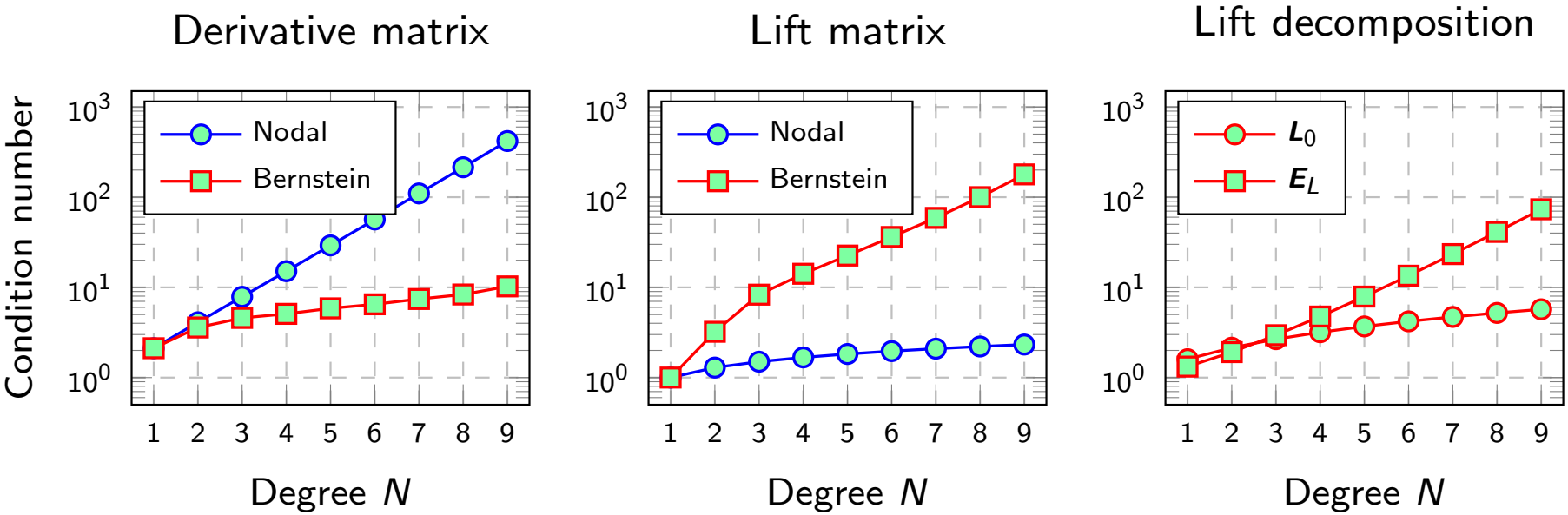

Condition numbers of matrices for nodal and Bernstein-Bezier bases.

Numerical stability of Bernstein-Bezier DG

- Conditioning of derivative, lift matrices comparable to nodal basis.

$$\kappa(\mathbf{A}) = \frac{\sigma_1}{\sigma_r}$$

- Comparable long-time growth of (single precision) numerical error.

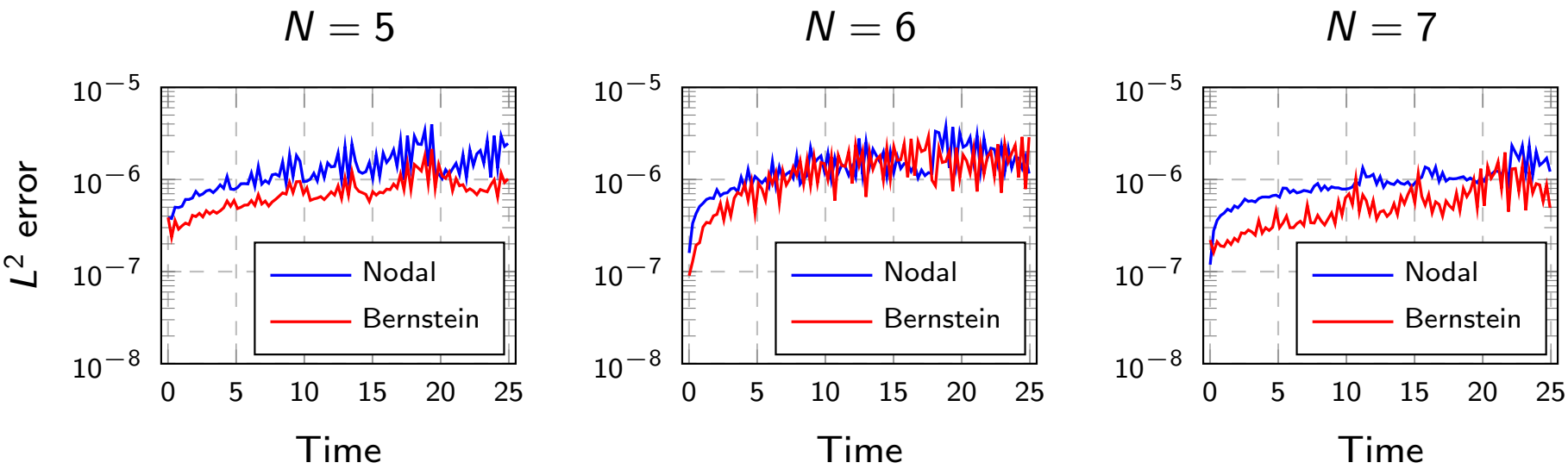

Evolution of L^2 error (acoustics) for nodal and Bernstein-Bezier bases.

GPU runtime comparison of BBDG and nodal DG

Bernstein-Bezier DG achieves $\approx 2\times$ speedup at moderate orders, and up to $\approx 6\times$ speedup at high orders.

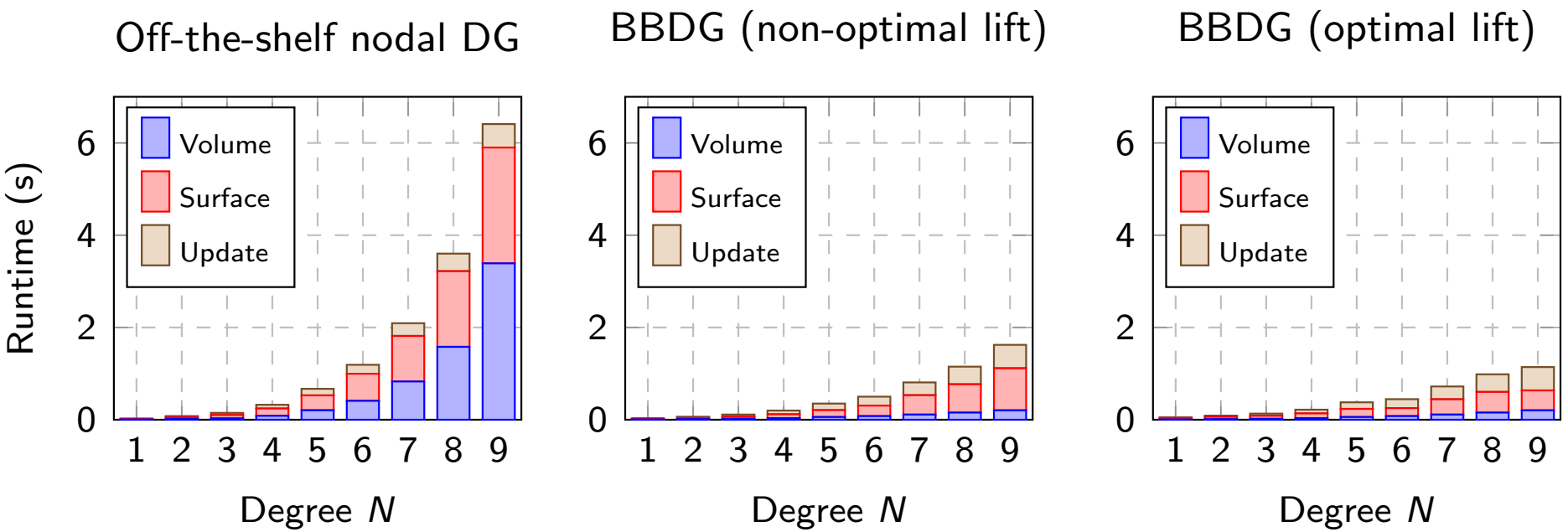

$$\underbrace{\frac{\mathrm{d}\mathbf{u}}{\mathrm{d}t}}_{\text{Update kernel}} = \underbrace{\mathbf{D}_x\mathbf{u}}_{\text{Volume kernel}} + \underbrace{\sum_{\text{faces}} \mathbf{L}_f\,(\text{flux})}_{\text{Surface kernel}}, \quad \mathbf{L}_f = \mathbf{M}^{-1}\mathbf{M}_f.$$

GPU runtime comparison of BBDG and nodal DG

Bernstein-Bezier DG achieves $\approx 2\times$ speedup at moderate orders, and up to $\approx 6\times$ speedup at high orders.

BB speedup (non-opt. lift) over nodal

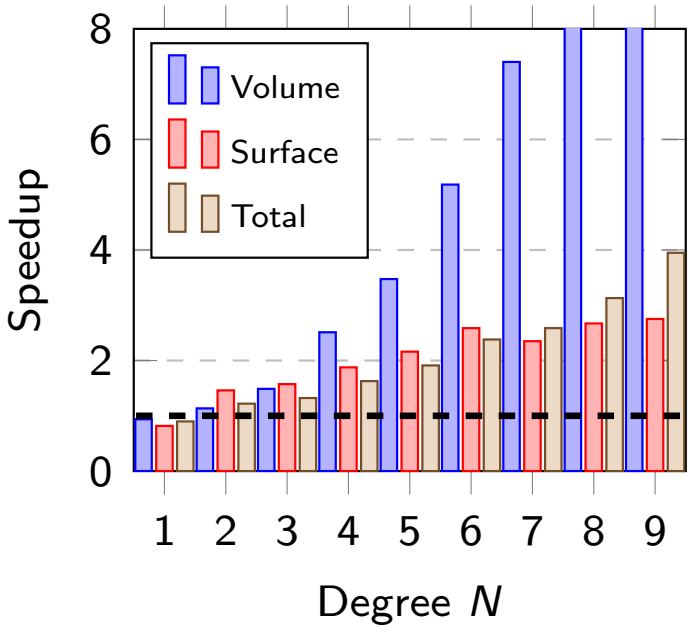

BB speedup (optimal lift) over nodal

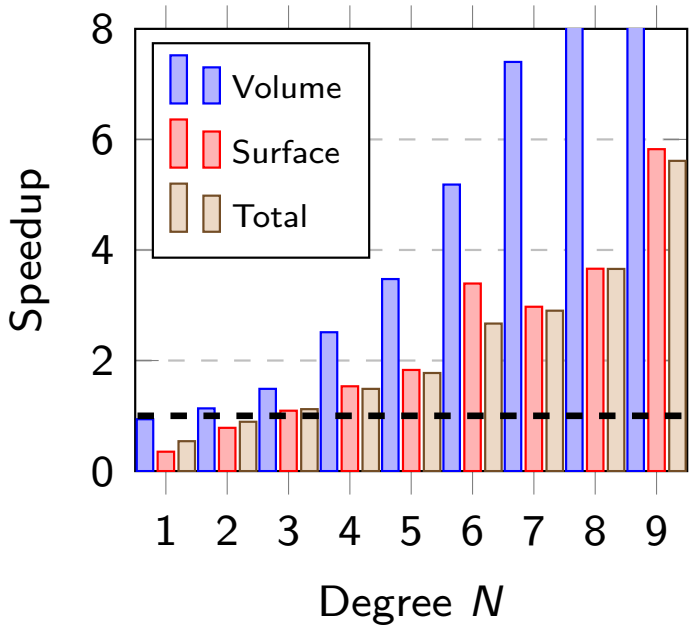

$$\underbrace{\frac{\mathrm{d}\mathbf{u}}{\mathrm{d}t}}_{\text{Update kernel}} = \underbrace{\mathbf{D}_x\mathbf{u}}_{\text{Volume kernel}} + \underbrace{\sum_{\text{faces}} \mathbf{L}_f\,(\text{flux})}_{\text{Surface kernel}}, \quad \mathbf{L}_f = \mathbf{M}^{-1}\mathbf{M}_f.$$

Outline

Energy stable discontinuous Galerkin formulations

- Model problem: acoustic wave equation

$$\frac{1}{c^2}\frac{\partial p}{\partial t} = \nabla \cdot \boldsymbol{u}, \qquad \frac{\partial \boldsymbol{u}}{\partial t} = \nabla p$$

- (Local) formulation with penalty fluxes

$$\int_{D^k} \frac{1}{c^2}\frac{\partial p}{\partial t} q = \int_{D^k} \nabla \cdot \boldsymbol{u} q + \frac{1}{2}\int_{\partial D^k} \left([\![\boldsymbol{u}]\!] \cdot \boldsymbol{n} + \tau_p [\![p]\!] \right) q$$

$$\int_{D^k} \frac{\partial \boldsymbol{u}}{\partial t} \boldsymbol{v} = \int_{D^k} \nabla p \cdot \boldsymbol{v} + \frac{1}{2}\int_{\partial D^k} \left([\![p]\!] + \tau_u [\![\boldsymbol{u}]\!] \cdot \boldsymbol{n} \right) \boldsymbol{v}$$

- High order accuracy, semi-discrete energy stability

$$\frac{\partial}{\partial t}\left(\sum_k \int_{D^k} \frac{p^2}{c^2} + |\boldsymbol{u}|^2 \right) = -\sum_k \int_{\partial D^k} \tau_p [\![p]\!]^2 + \tau_u [\![\boldsymbol{u} \cdot \boldsymbol{n}]\!]^2 \leq 0.$$

High order approximation of media and geometry

- Efficient implementation on **simplicial** meshes: c^2 piecewise constant, non-curved meshes (J, J^f piecewise constant).

$$\int_{D^k} \frac{1}{c^2} \frac{\partial p}{\partial t} q = \int_{D^k} \nabla \cdot \boldsymbol{u} q + \frac{1}{2} \int_{\partial D^k} (\llbracket \boldsymbol{u} \rrbracket \cdot \boldsymbol{n} + \tau_p \llbracket p \rrbracket) q$$

$$\int_{D^k} \frac{\partial \boldsymbol{u}}{\partial t} \boldsymbol{v} = \int_{D^k} \nabla p \cdot \boldsymbol{v} + \frac{1}{2} \int_{\partial D^k} (\llbracket p \rrbracket + \tau_u \llbracket \boldsymbol{u} \rrbracket \cdot \boldsymbol{n}) \boldsymbol{v}$$

- Spurious reflections for low order approximations of media, geometry.

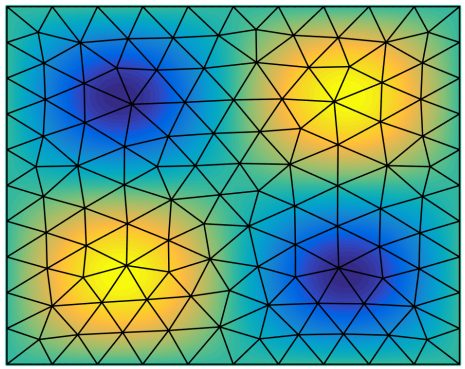

(a) Mesh and exact c^2

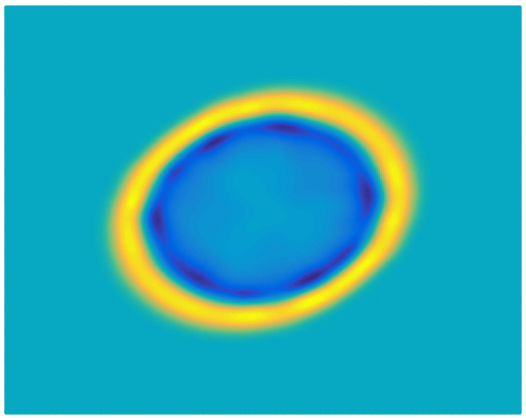

(b) Piecewise const. c^2

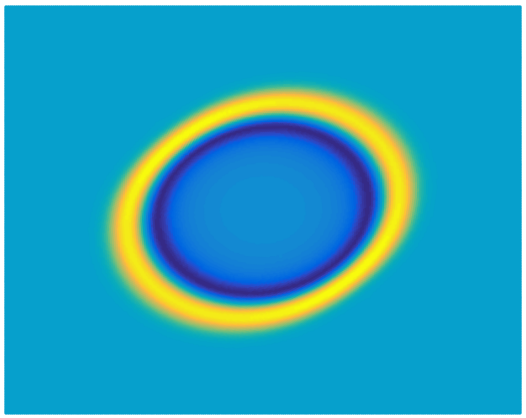

(c) High order c^2

High order approximation of media and geometry

- Efficient implementation on **simplicial** meshes: c^2 piecewise constant, non-curved meshes (J, J^f piecewise constant).

$$\int_{\widehat{D}} \frac{1}{c^2} \frac{\partial p}{\partial t} q J = \int_{\widehat{D}} \nabla \cdot \boldsymbol{u} q J + \frac{1}{2} \int_{\partial \widehat{D}} \left([\![\boldsymbol{u}]\!] \cdot \boldsymbol{n} + \tau_p [\![p]\!] \right) q J^f$$

$$\int_{\widehat{D}} \frac{\partial \boldsymbol{u}}{\partial t} \boldsymbol{v} J = \int_{\widehat{D}} \nabla p \cdot \boldsymbol{v} J + \frac{1}{2} \int_{\partial \widehat{D}} \left([\![p]\!] + \tau_u [\![\boldsymbol{u}]\!] \cdot \boldsymbol{n} \right) \boldsymbol{v} J^f$$

- Spurious reflections for low order approximations of media, geometry.

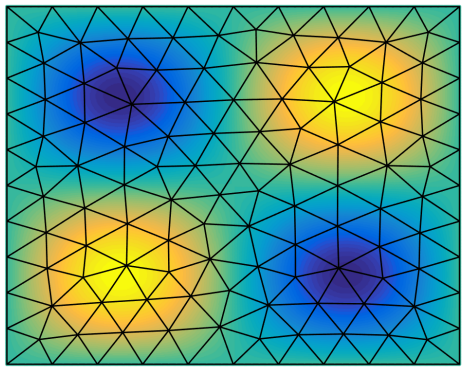

(a) Mesh and exact c^2

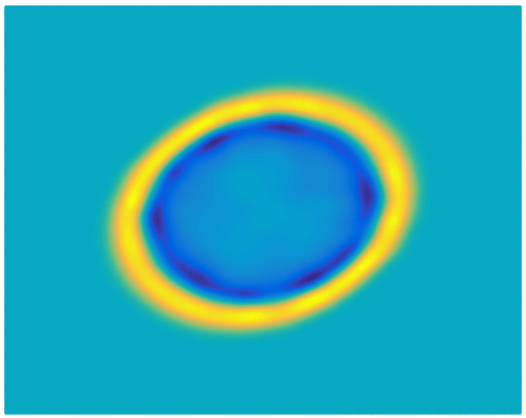

(b) Piecewise const. c^2

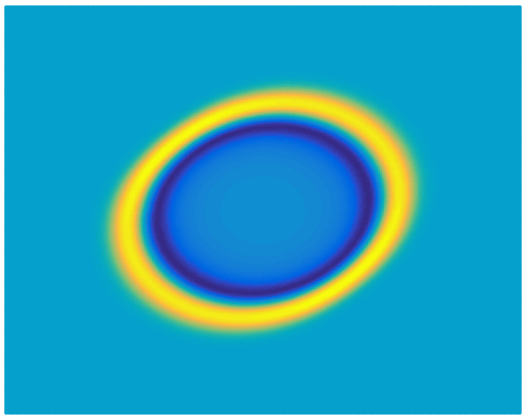

(c) High order c^2

High order approximation of media and geometry

- Efficient implementation on **simplicial** meshes: c^2 piecewise constant, non-curved meshes (J, J^f piecewise constant).

$$\frac{J}{c^2}\int_{\widehat{D}} \frac{\partial p}{\partial t} q = J\int_{\widehat{D}} \nabla\cdot \boldsymbol{u} q + J^f \frac{1}{2}\int_{\partial\widehat{D}} \left(\llbracket \boldsymbol{u}\rrbracket \cdot \boldsymbol{n} + \tau_p \llbracket p\rrbracket\right) q$$

$$J\int_{\widehat{D}} \frac{\partial \boldsymbol{u}}{\partial t} \boldsymbol{v} = J\int_{\widehat{D}} \nabla p\cdot \boldsymbol{v} + J^f \frac{1}{2}\int_{\partial\widehat{D}} \left(\llbracket p\rrbracket + \tau_u \llbracket \boldsymbol{u}\rrbracket \cdot \boldsymbol{n}\right) \boldsymbol{v}$$

- Spurious reflections for low order approximations of media, geometry.

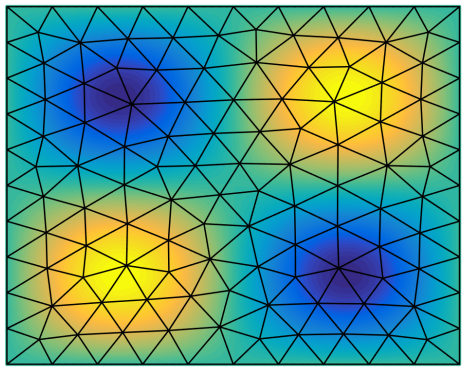

(a) Mesh and exact c^2

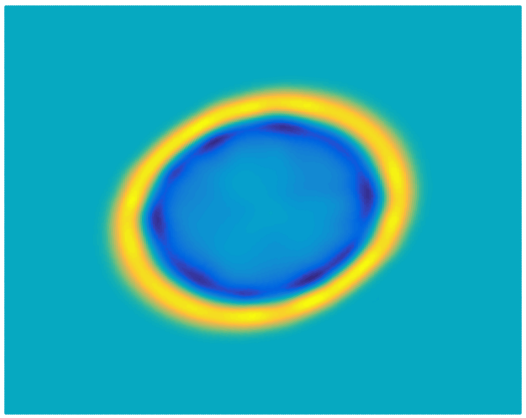

(b) Piecewise const. c^2

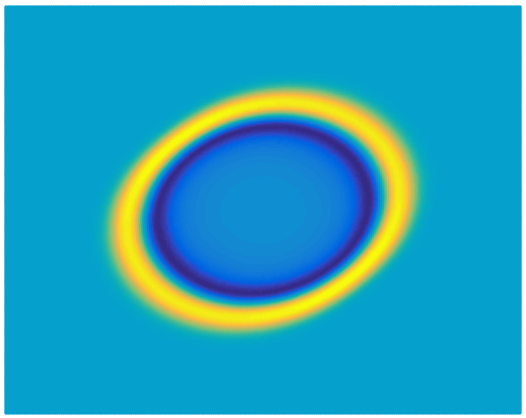

(c) High order c^2

Weighted mass matrices

- Spatially varying weights appear in DG mass matrices

$$\int_{\widehat{D}} \frac{1}{c^2}\frac{\partial p}{\partial t} q J = \text{pressure RHS}, \qquad \int_{\widehat{D}} \frac{\partial \boldsymbol{u}}{\partial t}\boldsymbol{v} J = \text{velocity RHS}$$

- Curvilinear meshes and wave propagation in heterogeneous media

$$(\boldsymbol{M}_w)_{ij} = \int_{\widehat{D}} \phi_i \phi_j w(x),$$

$$\frac{\mathrm{d}}{\mathrm{d}t}\boldsymbol{M}_w \boldsymbol{u} = \text{right hand side.}$$

- Inherits **high order accuracy** and **energy stability** with respect to a weighted L^2 norm, but requires $\boldsymbol{M}_w^{-1}$ explicitly over each element.
- On-the-fly assembly + inversion or pre-computation and storage.

Weighted mass matrices

- Spatially varying weights appear in DG mass matrices

$$\int_{\widehat{D}} \frac{1}{c^2}\frac{\partial p}{\partial t} q J = \text{pressure RHS}, \qquad \int_{\widehat{D}} \frac{\partial \boldsymbol{u}}{\partial t} \boldsymbol{v} J = \text{velocity RHS}$$

- Curvilinear meshes and wave propagation in heterogeneous media

$$(\boldsymbol{M}_w)_{ij} = \int_{\widehat{D}} \phi_i \phi_j J(x),$$

$$\frac{\mathrm{d}}{\mathrm{d}t} \boldsymbol{M}_J \boldsymbol{u} = \text{right hand side}.$$

- Inherits **high order accuracy** and **energy stability** with respect to a weighted L^2 norm, but requires $\boldsymbol{M}_w^{-1}$ explicitly over each element.
- On-the-fly assembly + inversion or pre-computation and storage.

Weighted mass matrices

- Spatially varying weights appear in DG mass matrices

$$\int_{\widehat{D}} \frac{1}{c^2} \frac{\partial p}{\partial t} q J = \text{pressure RHS}, \qquad \int_{\widehat{D}} \frac{\partial \boldsymbol{u}}{\partial t} \boldsymbol{v} J = \text{velocity RHS}$$

- Curvilinear meshes and wave propagation in heterogeneous media

$$(\boldsymbol{M}_w)_{ij} = \int_{\widehat{D}} \phi_i \phi_j \frac{J}{c^2(x)},$$

$$\frac{\mathrm{d}}{\mathrm{d}t} \boldsymbol{M}_{J/c^2} \boldsymbol{u} = \text{right hand side}.$$

- Inherits **high order accuracy** and **energy stability** with respect to a weighted L^2 norm, but requires $\boldsymbol{M}_w^{-1}$ explicitly over each element.

- On-the-fly assembly + inversion or pre-computation and storage.

Weighted mass matrices

- Spatially varying weights appear in DG mass matrices

$$\int_{\widehat{D}} \frac{1}{c^2}\frac{\partial p}{\partial t} q J = \text{pressure RHS}, \qquad \int_{\widehat{D}} \frac{\partial \boldsymbol{u}}{\partial t} \boldsymbol{v} J = \text{velocity RHS}$$

- Curvilinear meshes and wave propagation in heterogeneous media

$$(\boldsymbol{M}_w)_{ij} = \int_{\widehat{D}} \phi_i \phi_j w(x),$$

$$\frac{\mathrm{d}}{\mathrm{d}t} \boldsymbol{M}_w \boldsymbol{u} = \text{right hand side}.$$

- Inherits **high order accuracy** and **energy stability** with respect to a weighted L^2 norm, but requires $\boldsymbol{M}_w^{-1}$ explicitly over each element.
- On-the-fly assembly + inversion or pre-computation and storage.

Weight-adjusted DG: convergence and implementation

- Weight-adjusted DG (WADG): energy stable approximation of weighted mass matrix

$$\frac{\mathrm{d}}{\mathrm{d}t}\boldsymbol{M}_w\boldsymbol{u} \approx \frac{\mathrm{d}}{\mathrm{d}t}\boldsymbol{M}\left(\boldsymbol{M}_{1/w}\right)^{-1}\boldsymbol{M}\boldsymbol{u} = \text{right hand side.}$$

- WADG *a-priori* estimates: standard DG $O\left(h^{N+1/2}\right)$ convergence of L^2 error based on optimal weighted projection estimate:

$$\|u - P_w u\|_{L^2} \leq Ch^{N+1} \|w\|_{W^{N+1,\infty}} \left\| \frac{\sqrt{J}}{w} \right\|_{L^\infty} \|u\|_{W^{N+1,2}}.$$

- Bypasses inverse of weighted matrix $(\boldsymbol{M}_w)^{-1}$

$$\left(\boldsymbol{M}\left(\boldsymbol{M}_{1/w}\right)^{-1}\boldsymbol{M}\right)^{-1} = \boldsymbol{M}^{-1}\boldsymbol{M}_{1/w}\boldsymbol{M}^{-1}.$$

A non-intrusive and low-storage implementation

- Operator evaluation reuses implementation for $w = 1$

$$\boldsymbol{M}\left(\boldsymbol{M}_{1/w}\right)^{-1}\boldsymbol{M}\frac{\mathrm{d}\boldsymbol{U}}{\mathrm{d}t} = \boldsymbol{A}_h\boldsymbol{U}$$

$$\rightarrow \left(\boldsymbol{M}_{1/w}\right)^{-1}\boldsymbol{M}\frac{\mathrm{d}\boldsymbol{U}}{\mathrm{d}t} = \underbrace{\boldsymbol{M}^{-1}\boldsymbol{A}_h\boldsymbol{U}}_{\text{RHS for } w=1}$$

- Low storage: matrix-free application of $\boldsymbol{M}^{-1}\boldsymbol{M}_{1/w}$.

$$\left(\boldsymbol{M}\right)^{-1}\boldsymbol{M}_{1/w}\text{RHS} = \underbrace{\widehat{\boldsymbol{M}}^{-1}\boldsymbol{V}_q^T W}_{\boldsymbol{P}_q}\operatorname{diag}\left(1/w\right)\boldsymbol{V}_q\left(\text{RHS}\right).$$

- Non-intrusive: modify RHS locally before update. For non-curved meshes, can combine with *optimal complexity* RHS evaluation.[1]

[1] Chan, Warburton 2015. GPU-accelerated Bernstein-Bezier discontinuous Galerkin methods for wave propagation.

Weight-adjusted DG: not locally conservative

- Con: loss of local conservation for $w(x) \notin P^N$!
- Pro: superconvergence of conservation error

$$\text{Conservation error} \leq C h^{2N+2} \|w\|_{W^{N+1,\infty}} \|p\|_{W^{N+1,2}}$$

  where C depends on mesh quality and max/min values of w.

- Pro: can restore local conservation with rank-1 update (Shermann-Morrison).

Acoustic wave equation: heterogeneous media

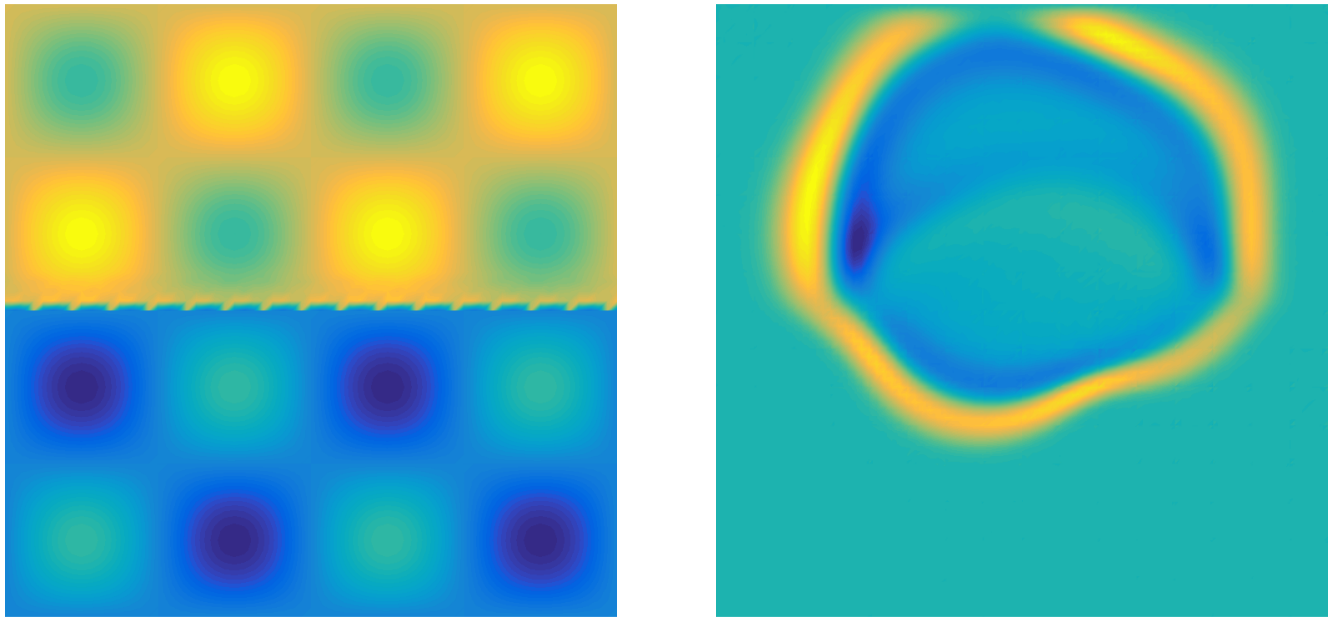

(a) $c^2(x, y)$ (b) Standard DG

Figure: Standard vs. weight-adjusted DG with spatially varying c^2 containing both smooth variations and a discontinuity.

Acoustic wave equation: heterogeneous media

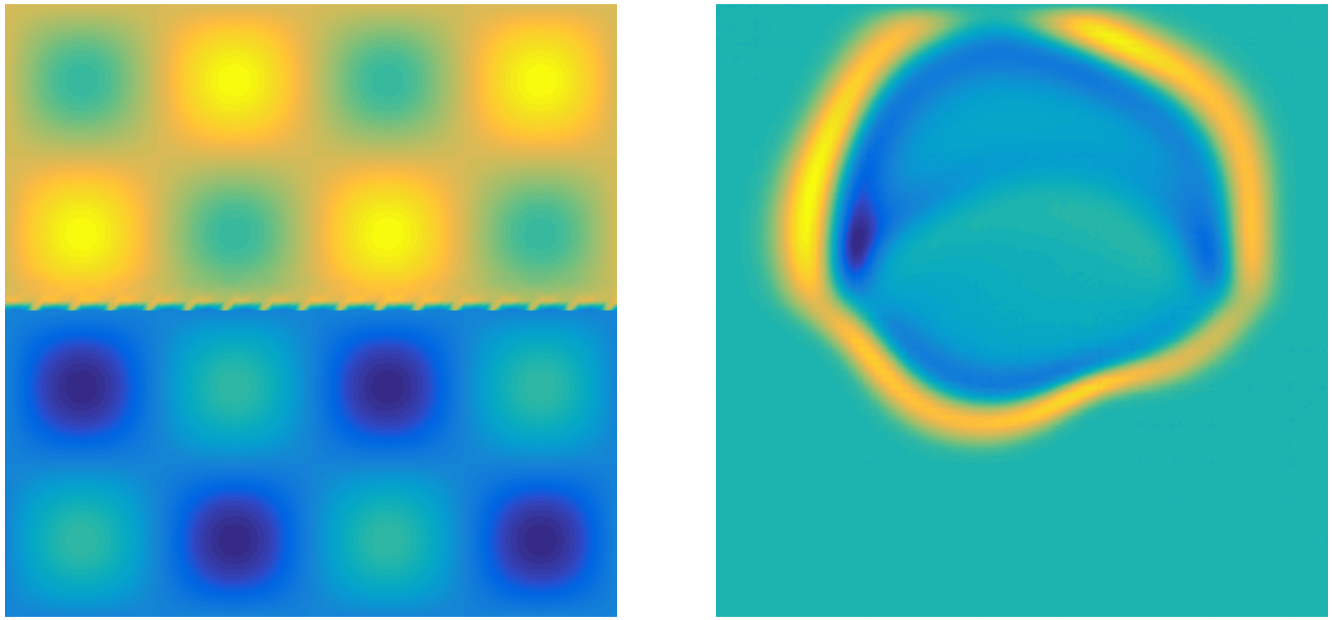

(a) $c^2(x, y)$ (b) Weighted-adjusted DG

Figure: Standard vs. weight-adjusted DG with spatially varying c^2 containing both smooth variations and a discontinuity.

Acoustics, variable coefficients: L^2 errors

Smooth wavefield $c^2(x,y) = 1 + \frac{1}{2}\sin(\pi x)\sin(\pi y)$

	$h = 1$	$h = 1/2$	$h = 1/4$	$h = 1/8$
DG $N = 1$	2.13e-01	6.25e-02	1.64e-02	4.19e-03
WADG $N = 1$	2.05e-01	5.99e-02	1.62e-02	4.18e-03
DG $N = 2$	3.01e-02	3.60e-03	4.21e-04	5.07e-05
WADG $N = 2$	2.89e-02	3.54e-03	4.18e-04	5.07e-05
DG $N = 3$	6.10e-03	3.33e-04	2.04e-05	1.22e-06
WADG $N = 3$	8.69e-03	3.47e-04	2.03e-05	1.22e-06
DG $N = 4$	6.61e-04	2.12e-05	6.39e-07	1.94e-08
WADG $N = 4$	1.09e-03	2.27e-05	6.30e-07	1.93e-08

Table: Convergence of standard, weight-adjusted DG to a manufactured solution.

Acoustics, variable coefficients: L^2 errors

Smooth wavefield $c^2(x,y) = 1 + \frac{1}{2}\sin(\pi x)\sin(\pi y)$

	$h = 1$	$h = 1/2$	$h = 1/4$	$h = 1/8$
DG $N = 1$	2.48e-01	7.58-02	1.69e-02	4.46e-03
WADG $N = 1$	2.50e-01	7.72e-02	1.69e-02	4.47e-03
DG $N = 2$	5.95e-02	9.95e-03	1.10e-03	1.22e-04
WADG $N = 2$	6.09e-02	1.02e-02	1.10e-03	1.22e-04
DG $N = 3$	2.29e-02	1.98e-03	9.52e-05	6.56e-06
WADG $N = 3$	1.98e-02	1.98e-03	9.52e-05	6.56e-06
DG $N = 4$	4.90e-03	3.01e-04	1.78e-05	7.27e-07
WADG $N = 4$	4.64e-03	3.02e-04	1.78e-05	7.28e-07

Table: Convergence to a reference solution ($N = 100$ spectral method).

Acoustics, variable coefficients: convergence

	$N = 1$	$N = 2$	$N = 3$	$N = 4$
DG	1.9220	3.0752	4.0440	5.0446
WADG	1.9211	3.0629	4.0752	5.0990

(a) Rates of convergence to manufactured solution

	$N = 1$	$N = 2$	$N = 3$	$N = 4$
DG	1.8256	3.1796	3.8589	4.6171
WADG	1.8425	3.1807	3.8583	4.6128

(b) Rates of convergence to reference solution

Observed L^2 rates between optimal $O(h^{N+1})$ and estimated $O(h^{N+1/2})$.

Outline

Weight-adjusted DG for curvilinear meshes

- Weight-adjusted L^2 projection $\tilde{P}_N$ on curved domains

$$\tilde{P}_N(u) := P_N\left(\frac{1}{J}P_N\left(uJ\right)\right).$$

  where P_N is the L^2 projection onto the reference element.

- L^2 estimates for weight-adjusted projection:

$$\left\|u-\tilde{P}_N u\right\|_{L^2\left(D^k\right)} \lesssim \left\|\frac{1}{\sqrt{J}}\right\|_{L^\infty}^2 \|J\|_{W^{N+1,\infty}\left(D^k\right)} h^{N+1} \|u\|_{W^{N+1,2}\left(D^k\right)}.$$

- High order Sobolev norm of J - implies that convergence can suffer for non-smooth mappings.

Behavior of weight-adjusted L^2 projection

Comparison with L^2 projection and Low-Storage Curvilinear DG

$$\tilde{\phi}_i = \frac{\phi_i}{\sqrt{J}}, \qquad \boldsymbol{M}_{ij} = \int_{D^k} \tilde{\phi}_j \tilde{\phi}_i J = \int_{\widehat{D}} \phi_j \phi_i = \widehat{\boldsymbol{M}}_{ij}.$$

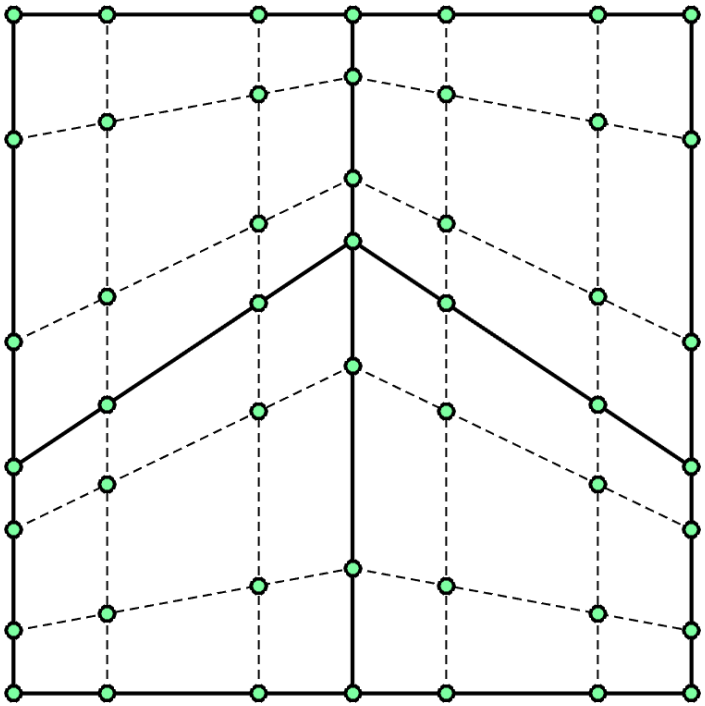

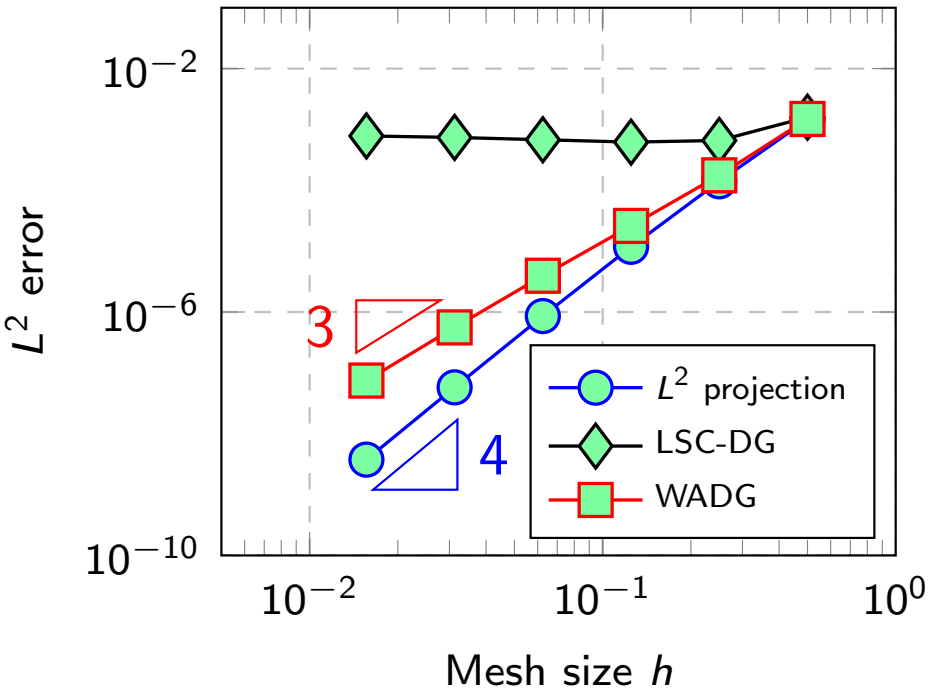

Figure: Arnold-type mesh with $\|J\|_{W^{N+1,\infty}} = O(h^{-1})$ for $N = 3$.

Behavior of weight-adjusted L^2 projection

Comparison with L^2 projection and Low-Storage Curvilinear DG

$$\tilde{\phi}_i = \frac{\phi_i}{\sqrt{J}}, \qquad \boldsymbol{M}_{ij} = \int_{D^k} \tilde{\phi}_j \tilde{\phi}_i J = \int_{\widehat{D}} \phi_j \phi_i = \widehat{\boldsymbol{M}}_{ij}.$$

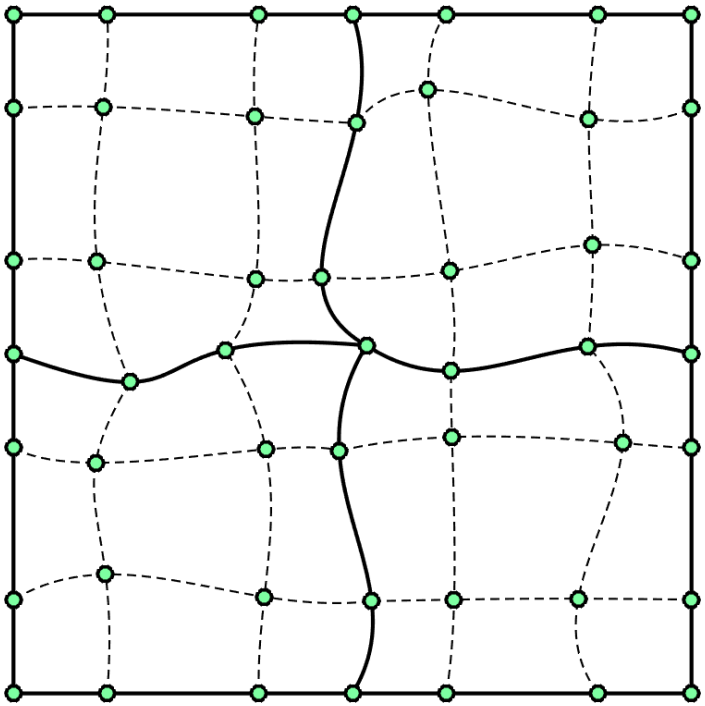

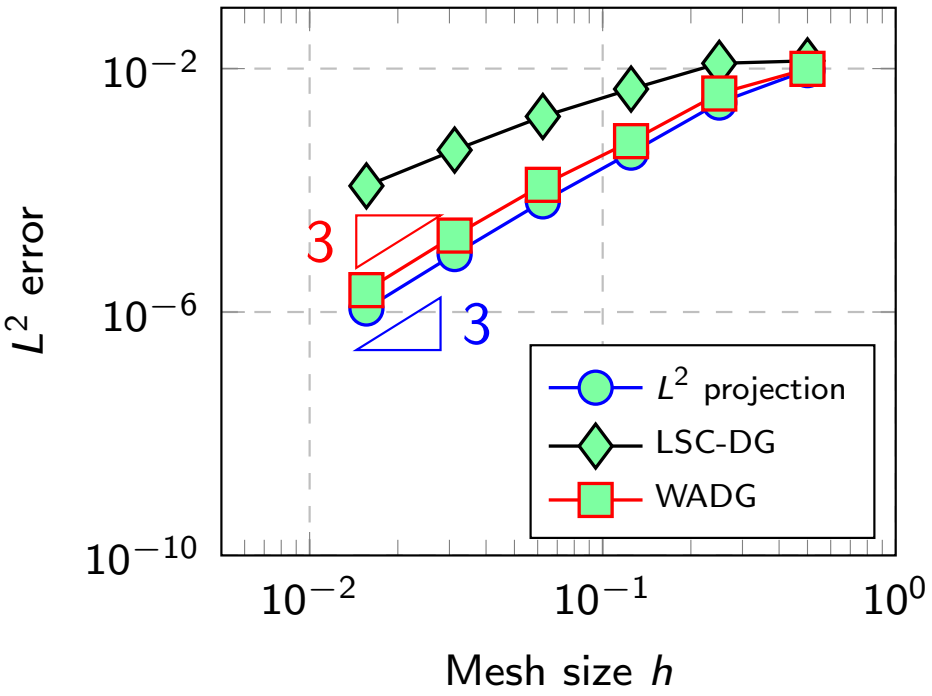

Figure: Curvilinear mesh constructed through random perturbation for $N = 3$.

Behavior of weight-adjusted L^2 projection

High order convergence slowed by growth of $\|J\|_{W^{N+1,\infty}} = O(h^N)$.

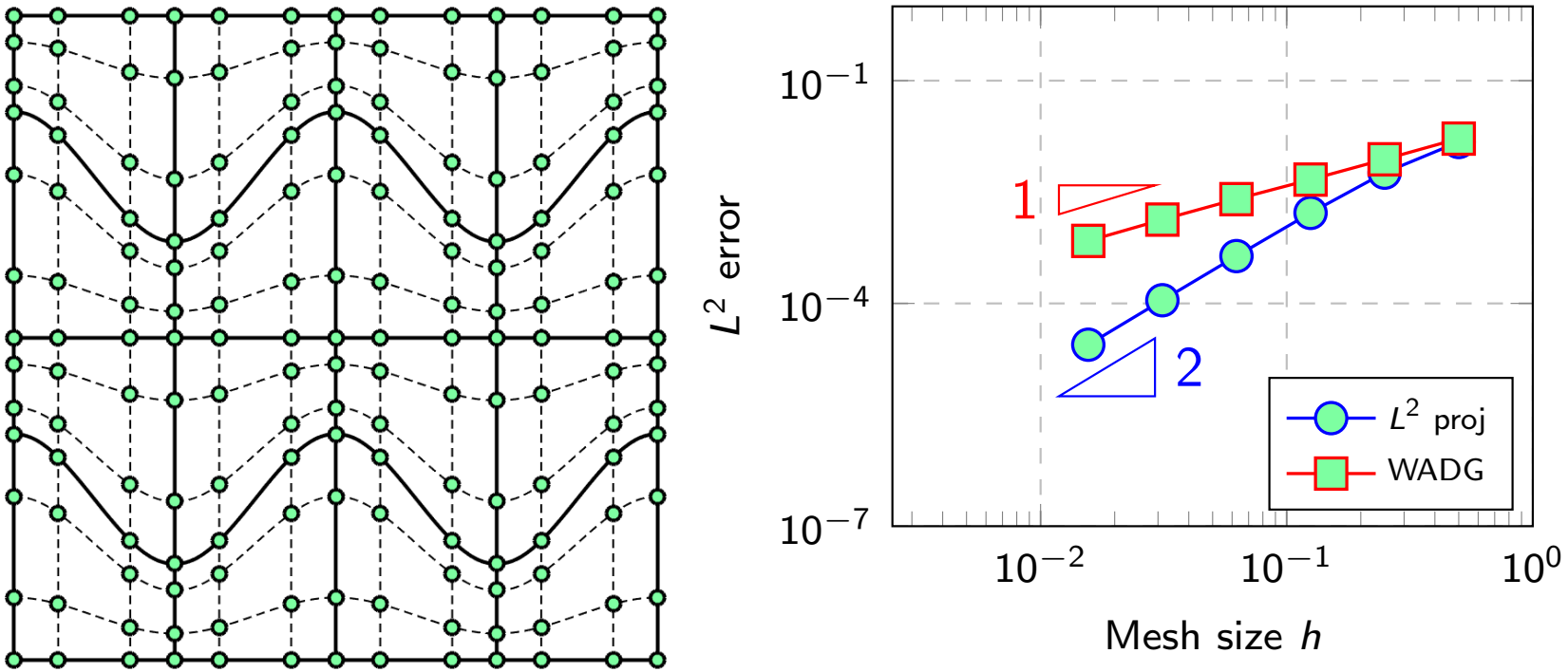

Figure: Moderately warped curved Arnold-type mesh for $N = 3$.

Behavior of weight-adjusted L^2 projection

High order convergence is stalled by growth of $\|J\|_{W^{N+1,\infty}} = O(h^{N+1})$.

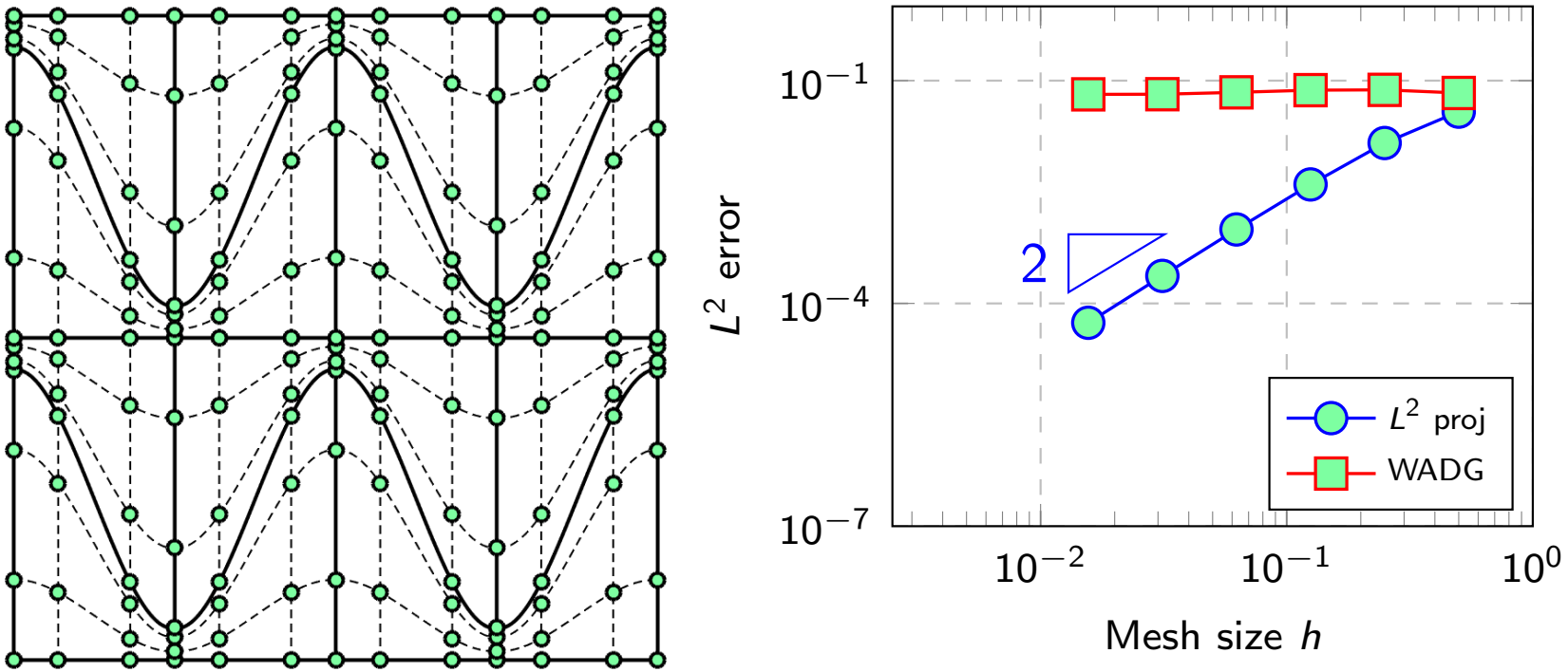

Figure: Heavily warped curved Arnold-type mesh for $N = 3$.

Curvilinear meshes: two-dimensional verification

Energy stability: quadrature-based skew-symmetric formulation.

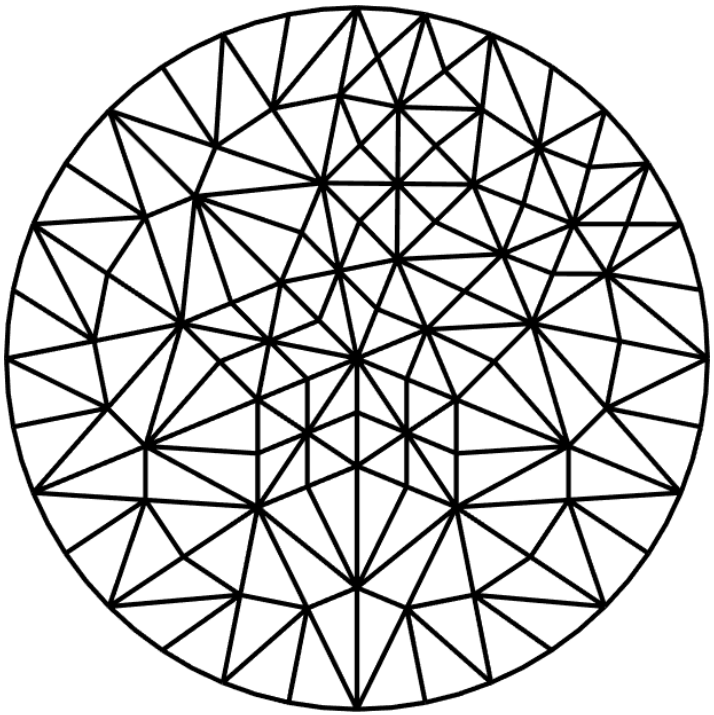

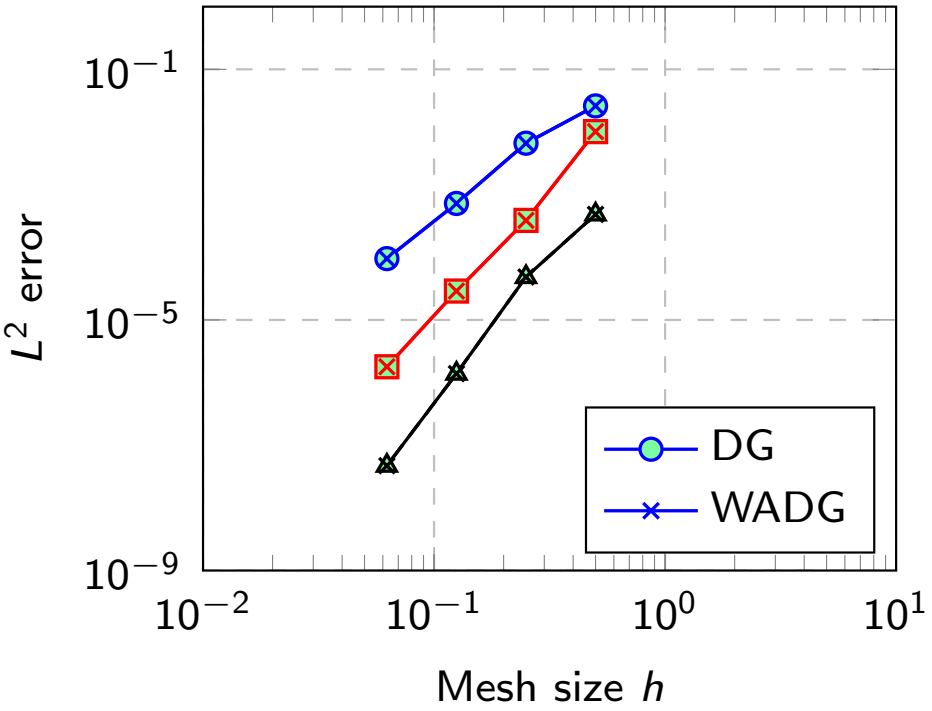

(a) L^2 errors for $N = 2, 3, 4$

Figure: Optimal L^2 convergence rates observed for curvilinear meshes.

Curvilinear meshes: DG eigenvalues (circular domain)

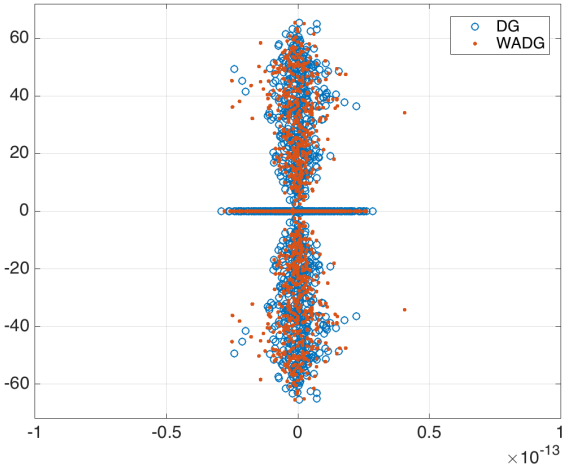

(a) Central fluxes

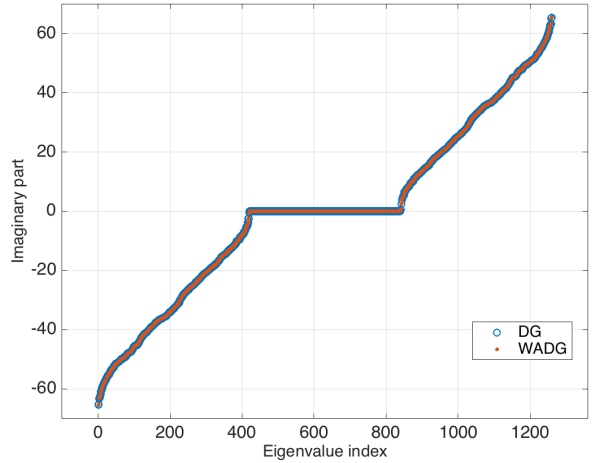

(b) $\mathrm{Im}\,(\lambda_i)$ for central fluxes

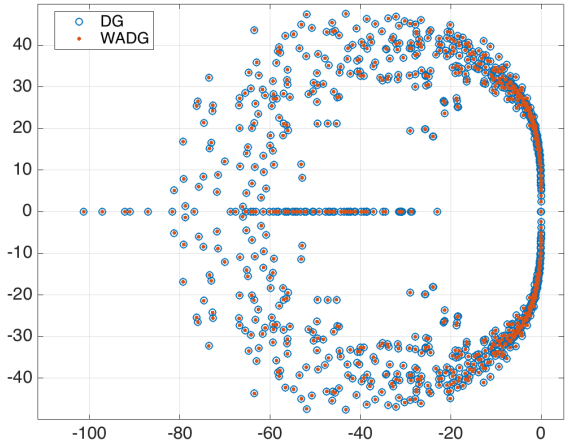

(c) Upwind fluxes

Curved meshes + heterogeneous media

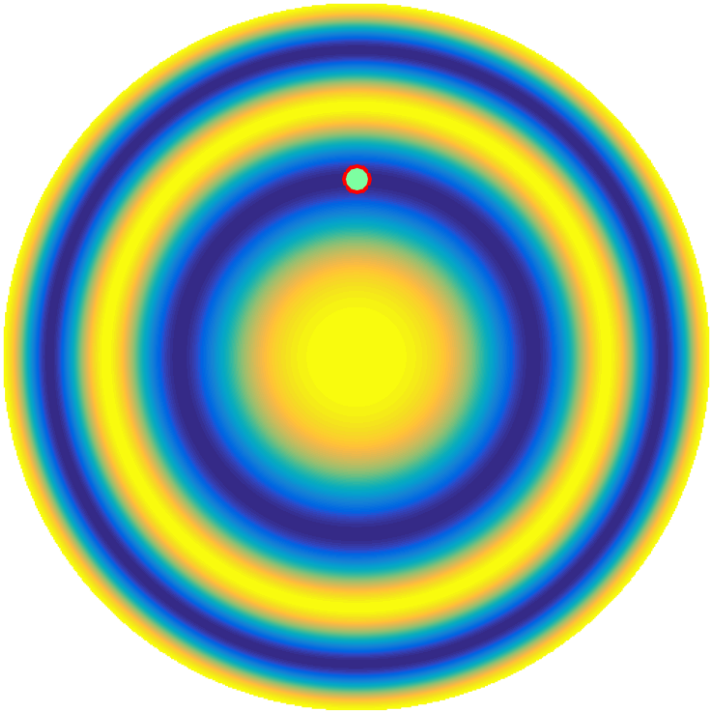

(a) Wavespeed $c^2(\boldsymbol{x})$

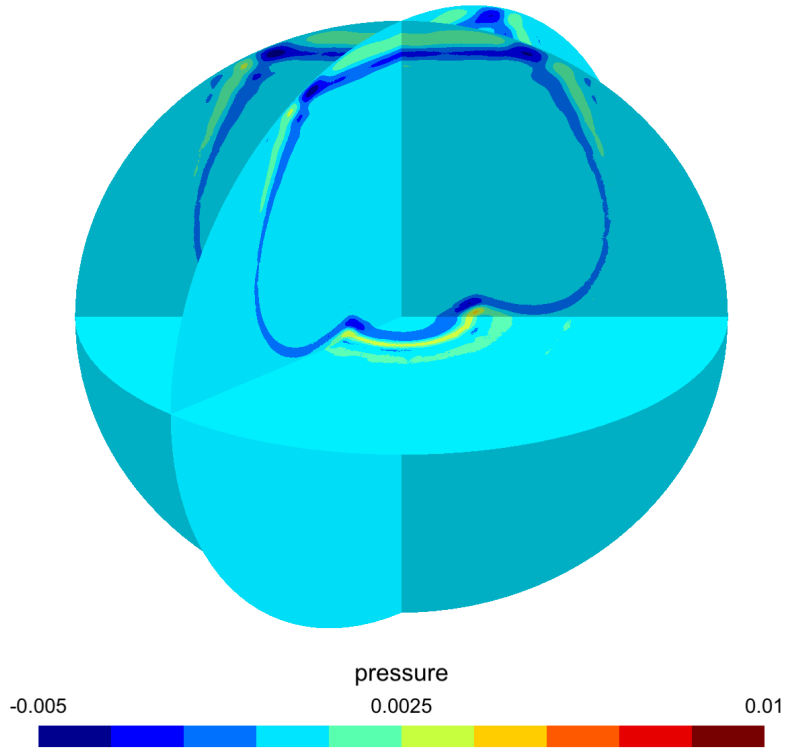

(b) Pressure isovalues at $t = .6$

Can incorporate heterogeneous media with curved elements at no additional cost.

Time-domain spline methods

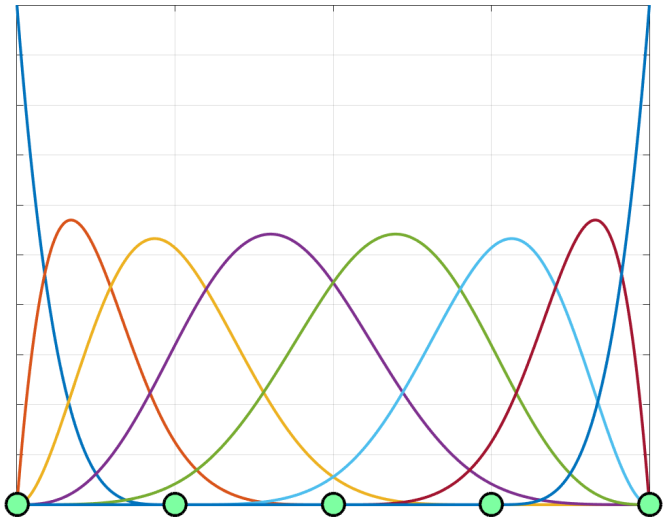

(a) Uniform knots

(b) Optimal knots

Figure: B-spline bases with uniform and optimal knot vectors ($N = 4, K = 4$).

- Optimal knots (at roots of specific eigenfunctions) minimize n-width.
- We approximate optimal knots using heuristic "smoothing".
- Lack of mass lumping: expensive to apply $\boldsymbol{M}^{-1}$.

Melkman and Micchelli 1978. Spline spaces are optimal for L^2 n-width.

Restoring Kronecker structure to M^{-1}

- Loss of Kronecker product structure in spline mass matrix inverses.
- WADG recovers tensor product: application of $\boldsymbol{M}_{1/J}$, $\widehat{\boldsymbol{M}}^{-1}$

$$\boldsymbol{M}_J^{-1} \approx \widehat{\boldsymbol{M}}^{-1} \boldsymbol{M}_{1/J} \widehat{\boldsymbol{M}}^{-1}$$
$$\widehat{\boldsymbol{M}}^{-1} = \widehat{\boldsymbol{M}}_{1\mathrm{D}}^{-1} \otimes \widehat{\boldsymbol{M}}_{1\mathrm{D}}^{-1} \otimes \widehat{\boldsymbol{M}}_{1\mathrm{D}}^{-1}.$$

- Maintains **provable** energy stability for general geometric mappings.
- Same approach has been used for Galerkin difference methods.

Mantzaflaris et al 2016. Low rank tensor methods in Galerkin-based IGA.

Banks and Hagstrom 2016. On Galerkin difference methods.

Approximation properties of optimal splines

- Improved (pre-asymptotic?) resolution for both oscillatory functions and non-affine mappings.
- Multi-patch IGA: optimal h-convergence rates (acoustics).

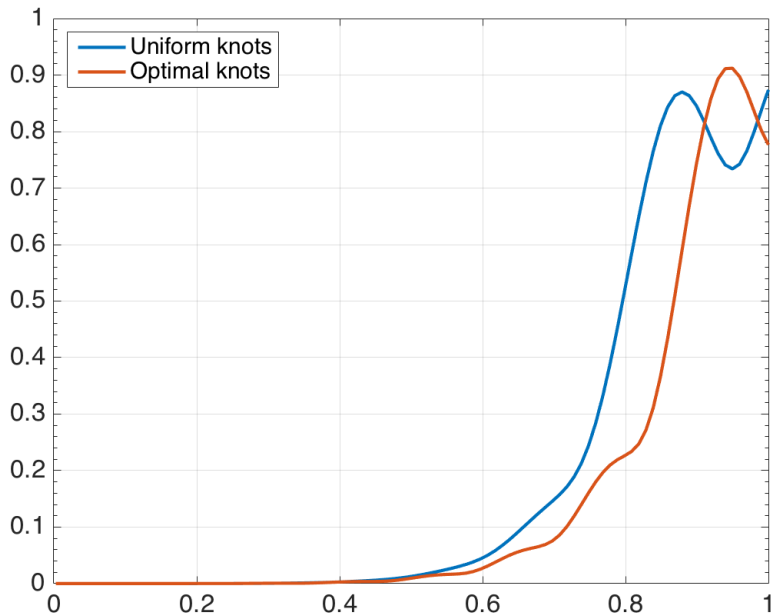

(a) L^2 error vs wavelengths (k) per dof

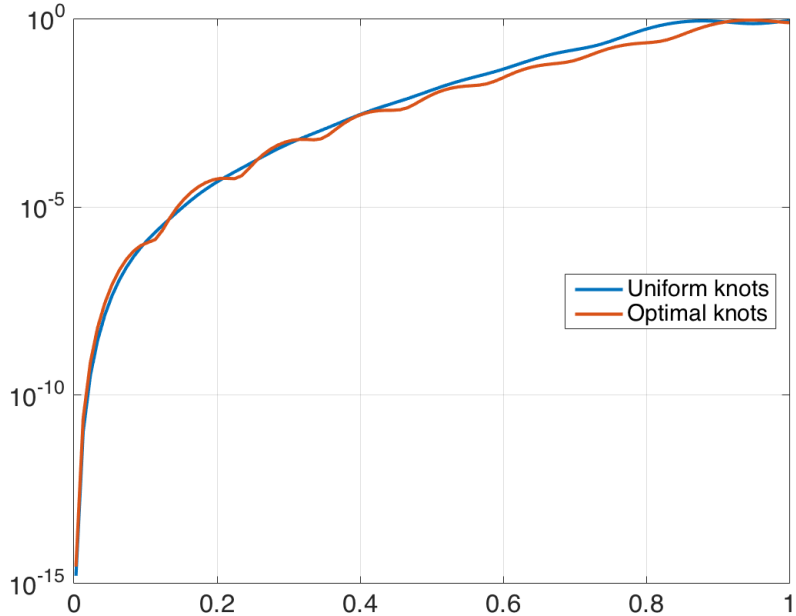

(b) Semi-log scale

Figure: L^2 error in approximating $u(x) = \cos\left(\frac{k\pi x}{2}\right)$ with $N = 4, K = 16$.

Approximation properties of optimal splines

- Improved (pre-asymptotic?) resolution for both oscillatory functions and non-affine mappings.
- Multi-patch IGA: optimal h-convergence rates (acoustics).

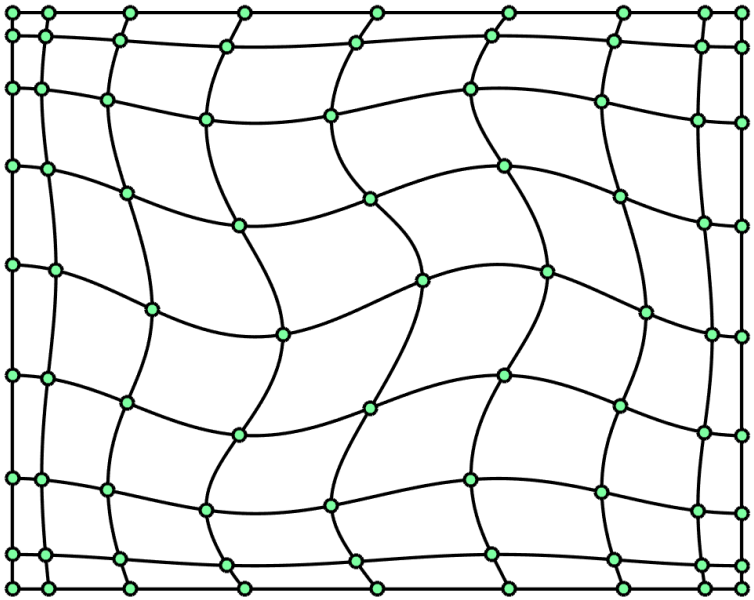

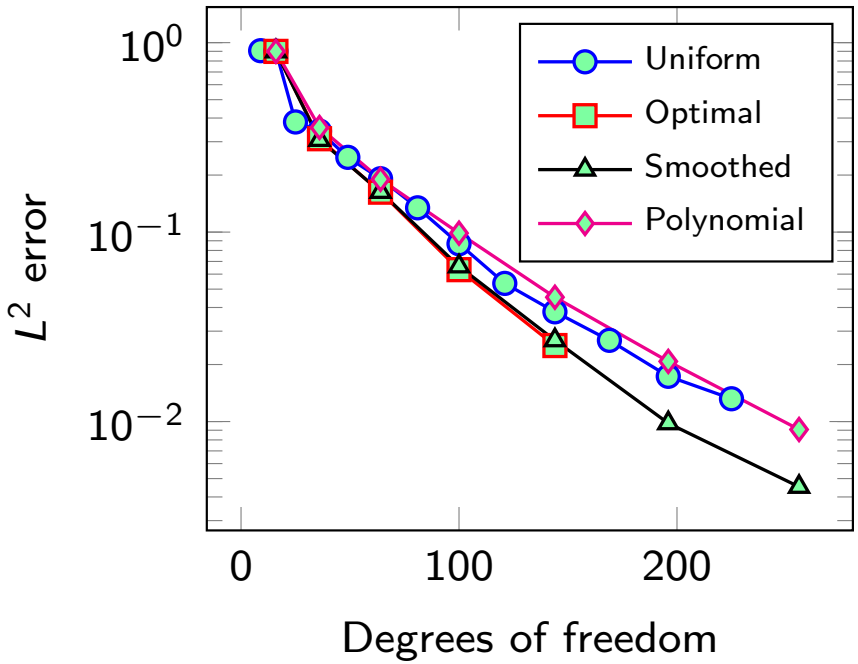

Figure: L^2 errors for $\cos\left(\frac{3\pi x}{2}\right)\cos\left(\frac{3\pi y}{2}\right)$ under degree refinement $N = 2, \ldots, 8$, using spline spaces with $K = N$ elements.

Application to IGA and time-domain wave propagation

- Bound $\rho(\boldsymbol{A}_h)$ using generalized Rayleigh quotients (Bendixon-Hirsch): depends on h and **constants** C_T, C_I.
- CFL: $O(h/N^2)$ for polynomials, $O(h/N)$ for splines if $h \geq O(1/N)$.

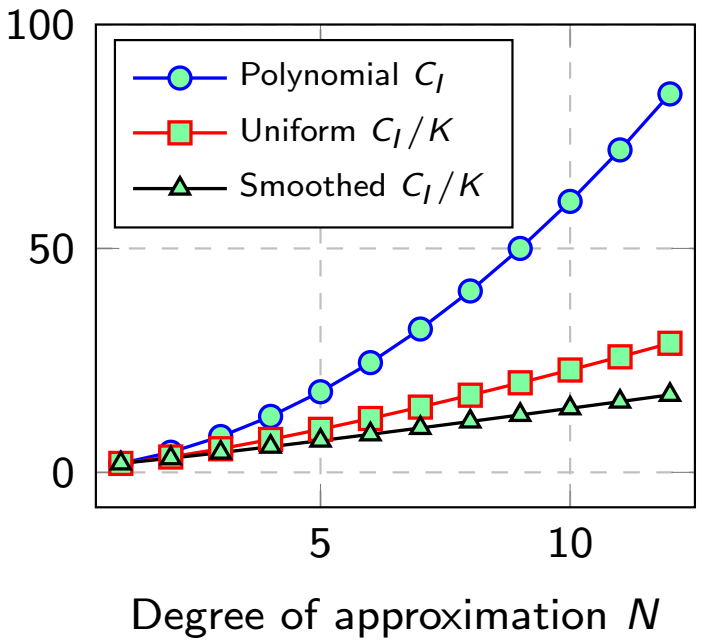

(a) Inverse inequality, $K = 2N$

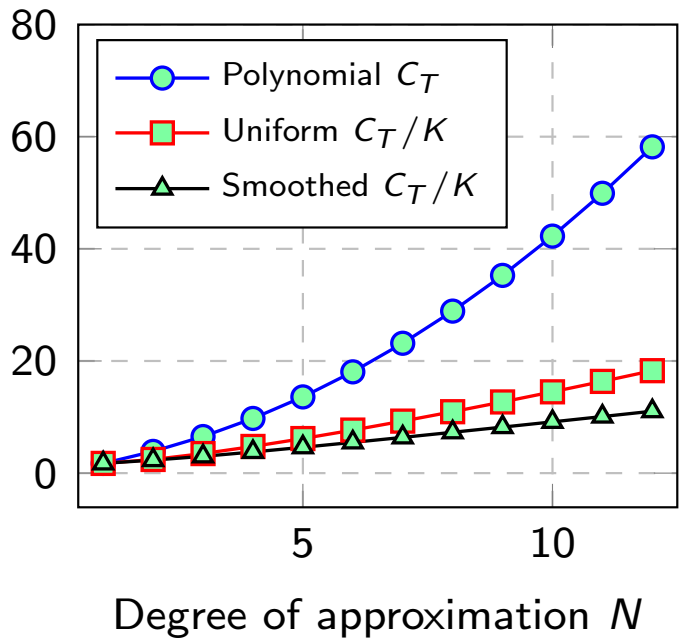

(b) Trace inequality, $K = 2N$

Outline

Matrix-valued weights and elastic wave propagation

- Symmetric velocity-stress form of linear elasticity ($\boldsymbol{A}_i$ constant)

$$\rho \frac{\partial \boldsymbol{v}}{\partial t} = \sum_{i=1}^{d} \boldsymbol{A}_i^T \frac{\partial \boldsymbol{\sigma}}{\partial \boldsymbol{x}_i}, \qquad \boldsymbol{C}^{-1} \frac{\partial \boldsymbol{\sigma}}{\partial t} = \sum_{i=1}^{d} \boldsymbol{A}_i \frac{\partial \boldsymbol{v}}{\partial \boldsymbol{x}_i}.$$

- DG formulation based on penalty fluxes, matrix-weighted mass matrix

$$(\boldsymbol{M}_{\boldsymbol{C}^{-1}})^{-1} = \begin{pmatrix} \boldsymbol{M}_{C_{11}^{-1}} & \cdots & \boldsymbol{M}_{C_{1d}^{-1}} \\ \vdots & \ddots & \vdots \\ \boldsymbol{M}_{C_{d1}^{-1}} & \cdots & \boldsymbol{M}_{C_{dd}^{-1}} \end{pmatrix}$$

- Weight-adjusted approximation for $\boldsymbol{C}^{-1}$ decouples into components

$$\boldsymbol{M}_{\boldsymbol{C}^{-1}}^{-1} \approx \left(\boldsymbol{I} \otimes \boldsymbol{M}^{-1}\right) \boldsymbol{M}_{\boldsymbol{C}} \left(\boldsymbol{I} \otimes \boldsymbol{M}^{-1}\right).$$

Hughes and Marsden 1978. Classical elastodynamics as a linear symmetric hyperbolic system.

Elastic wave propagation: convergence

- Convergence for harmonic oscillation, Rayleigh, Lamb, and Stoneley waves: between $O(h^{N+1})$ and $O(h^{N+1/2})$.
- $\boldsymbol{\sigma}$ error grows as $\left\|\boldsymbol{C}^{-1}\right\| \to \infty$ (e.g. incompressible limit $\lambda/\mu \to \infty$).

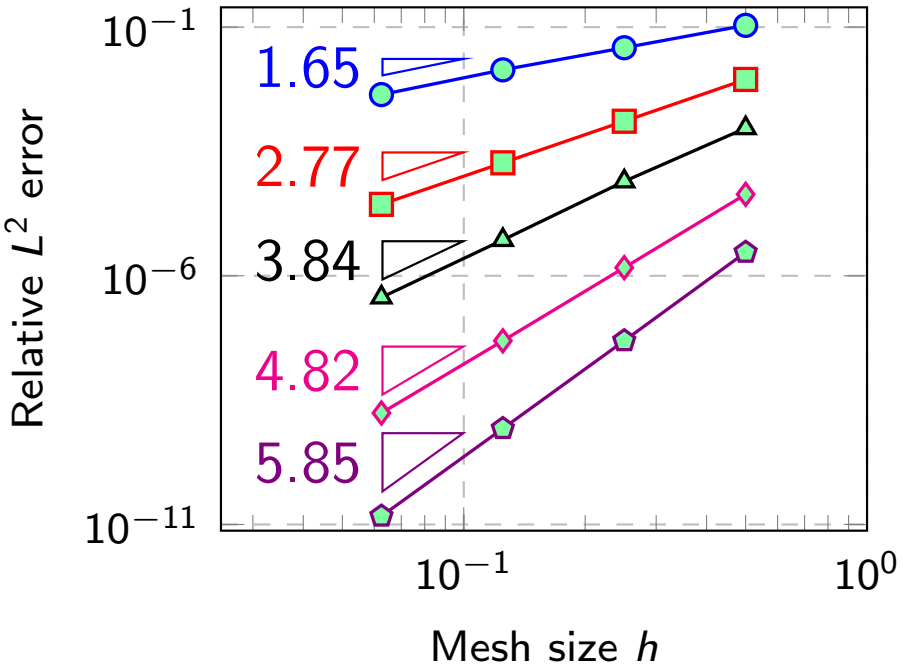

(a) Stoneley wave

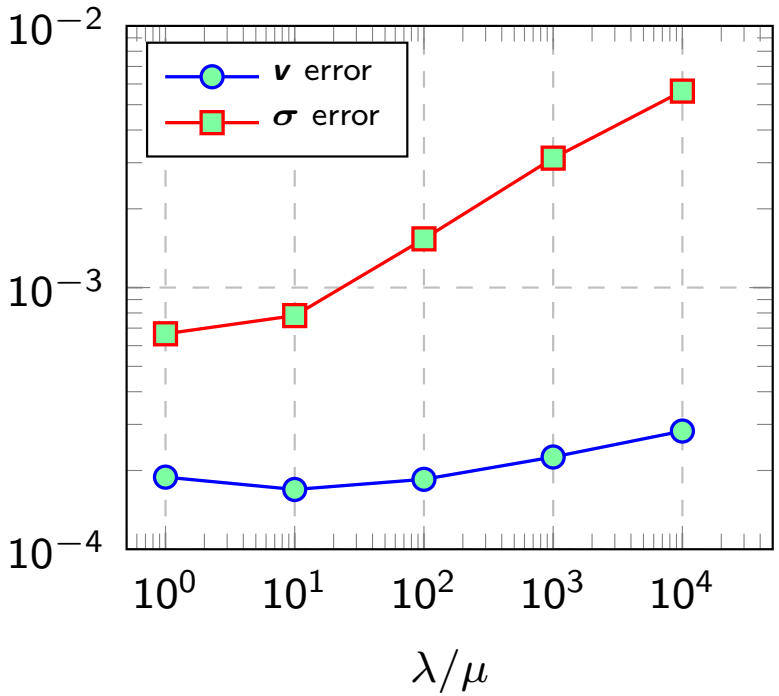

(b) $\left\|\boldsymbol{C}^{-1}\right\| \to \infty$, $N = 3, h = 1/8$.

Elastic wave propagation: anisotropy

No change in implementation for anisotropy - fluxes independent of $\boldsymbol{C}$.

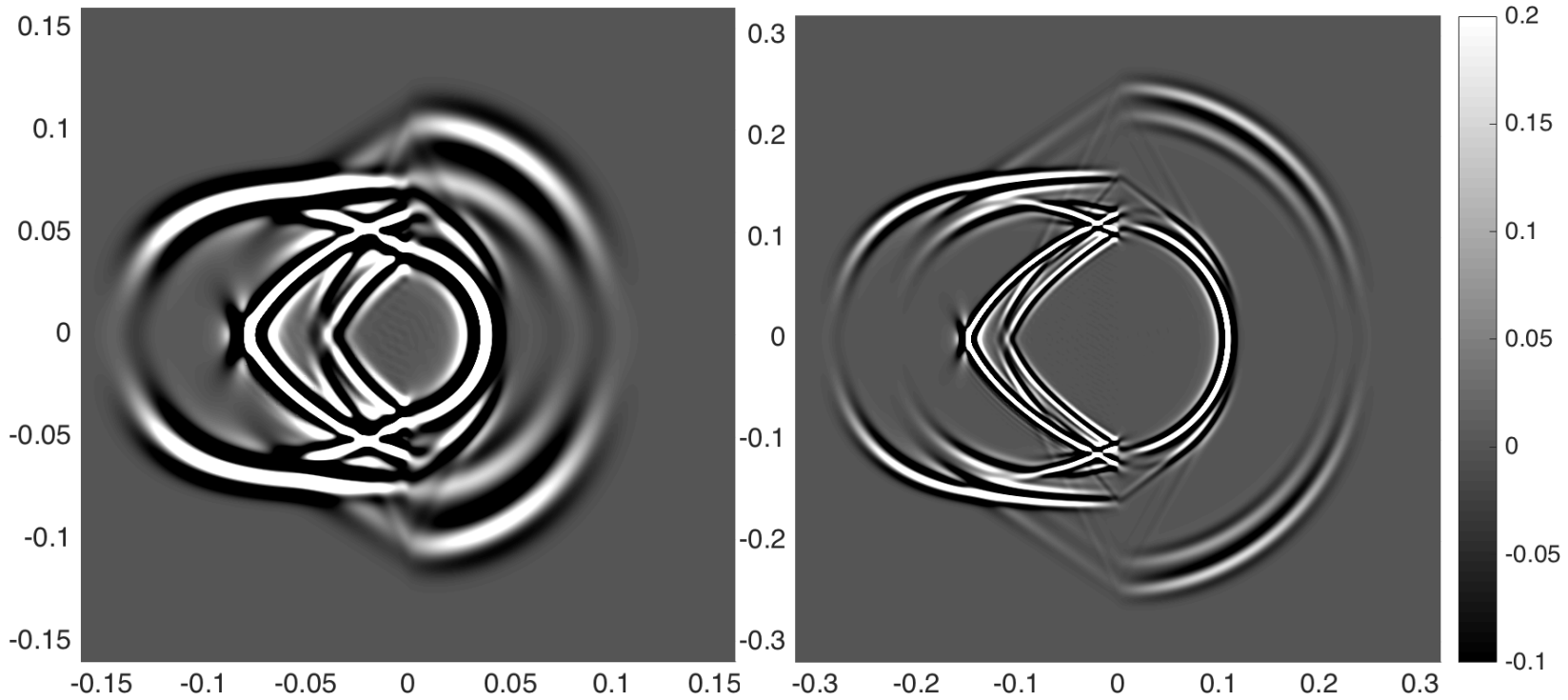

(a) Vertical velocity, $t = 30\mu s$ (b) Vertical velocity, $t = 60\mu s$

Figure: Heterogeneous media: transverse isotropy ($x < 0$) and isotropy ($x > 0$).

Komatitsch, Barnes, Tromp 2000. Simulation of anisotropic wave propagation based upon a spectral element method.

Elastic wave propagation: acoustic-elastic coupling

- Interface jumps become residuals of continuity conditions:

$$\boldsymbol{\sigma} \cdot \boldsymbol{n} = p\boldsymbol{n}, \qquad \boldsymbol{v} \cdot \boldsymbol{n} = \boldsymbol{u} \cdot \boldsymbol{n}.$$

- Energy stable for arbitrary heterogeneous media.

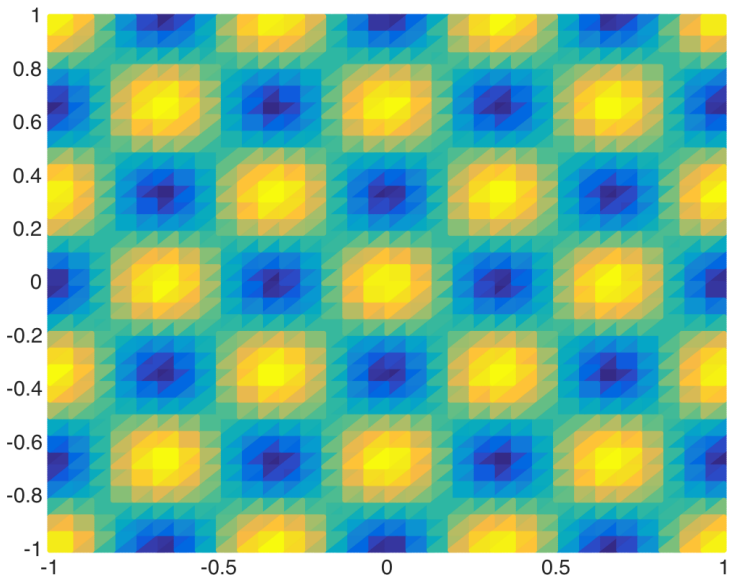

(a) Low order $c^2(\boldsymbol{x}), \mu(\boldsymbol{x})$

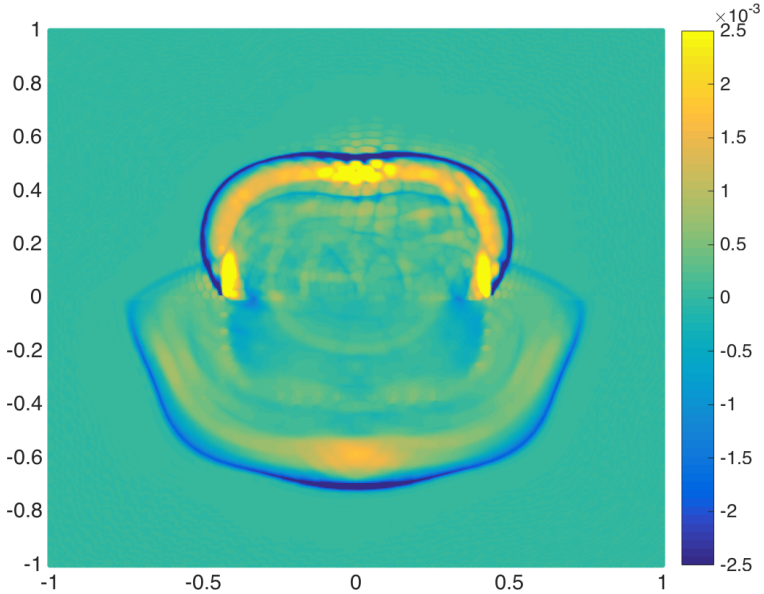

(b) $\mathrm{tr}(\boldsymbol{\sigma})$

Figure: Acoustic-elastic waves from a Ricker pulse ($N = 10$, $h = 1/16$).

Ye et al. 2016. A DG method with a modified penalty flux for the propagation and scattering of acousto-elastic waves.

Elastic wave propagation: acoustic-elastic coupling

- Interface jumps become residuals of continuity conditions:

$$\boldsymbol{\sigma} \cdot \boldsymbol{n} = p\boldsymbol{n}, \qquad \boldsymbol{v} \cdot \boldsymbol{n} = \boldsymbol{u} \cdot \boldsymbol{n}.$$

- Energy stable for arbitrary heterogeneous media.

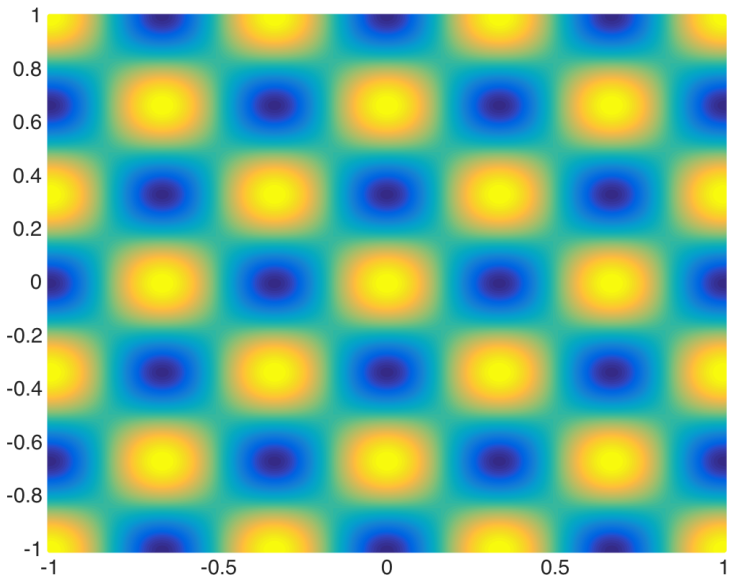

(a) High order $c^2(\boldsymbol{x}), \mu(\boldsymbol{x})$

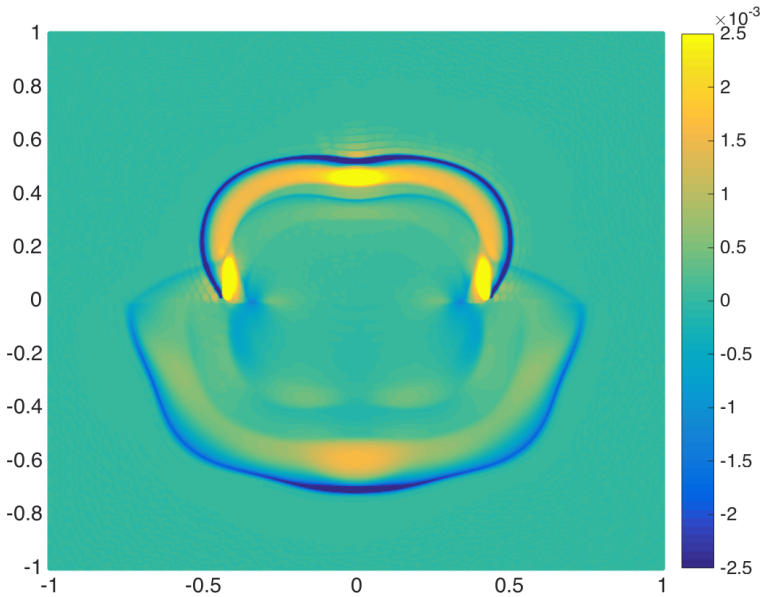

(b) $\mathrm{tr}(\boldsymbol{\sigma})$

Figure: Acoustic-elastic waves from a Ricker pulse ($N = 10$, $h = 1/16$).

Ye et al. 2016. A DG method with a modified penalty flux for the propagation and scattering of acousto-elastic waves.

Elastic wave propagation: 3D isotropic media

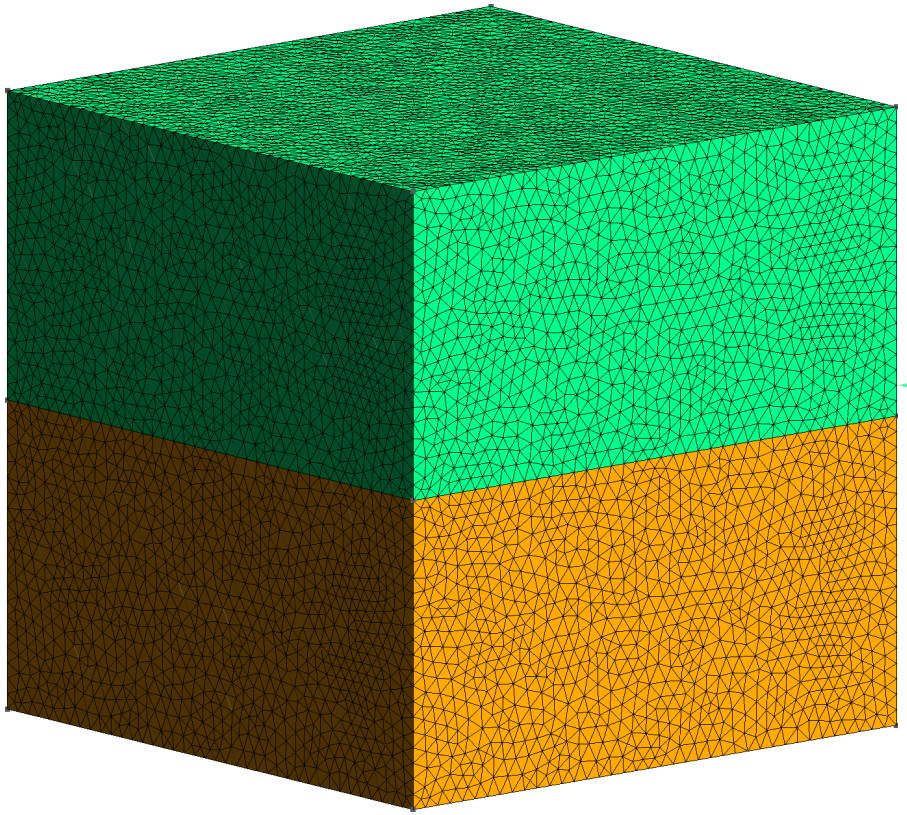

(a) Computational mesh

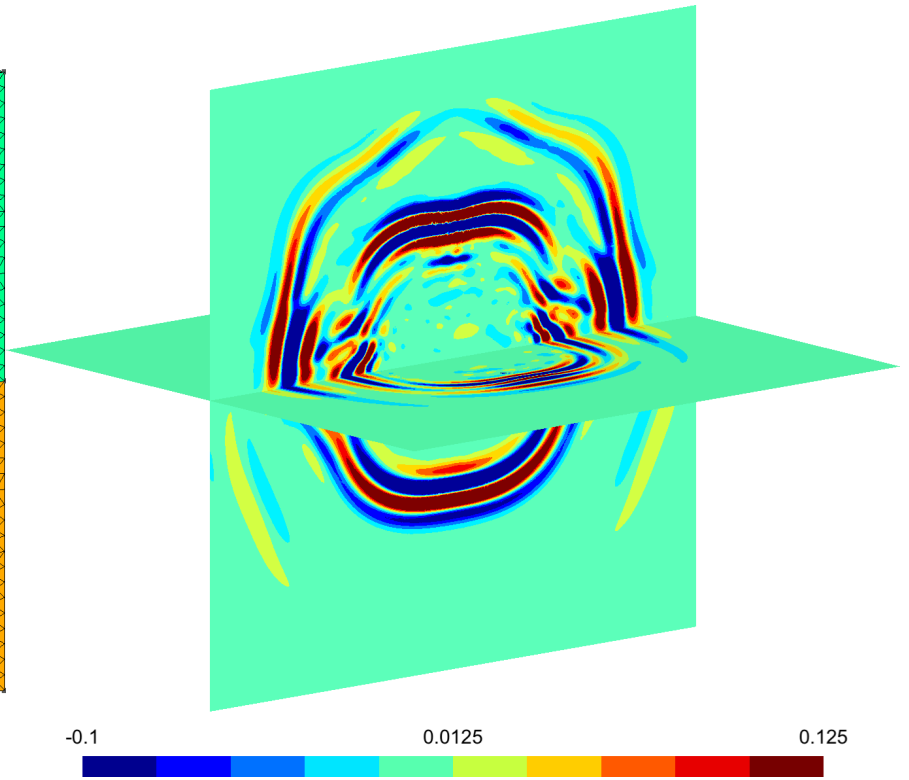

(b) Piecewise constant $\boldsymbol{C}(\boldsymbol{x})$

Figure: $\mathrm{tr}(\boldsymbol{\sigma})$ with $\mu(\boldsymbol{x}) = 1 + H(y) + \frac{1}{2}\cos(3\pi x)\cos(3\pi y)\cos(3\pi z)$, $N = 5$.

Elastic wave propagation: 3D isotropic media

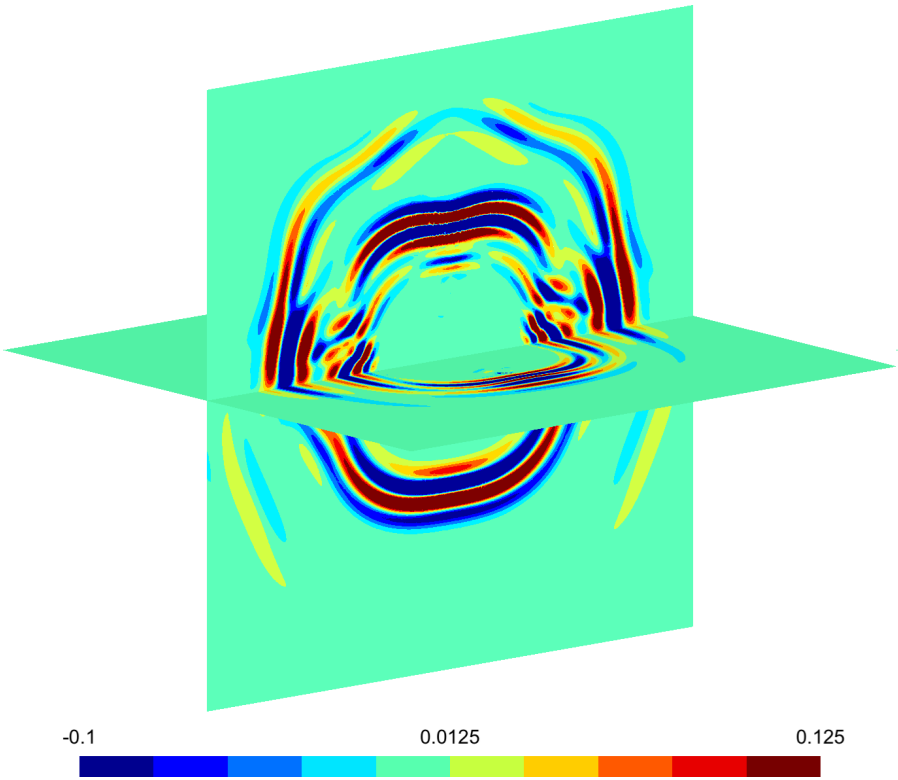

(a) High order $\boldsymbol{C}(\boldsymbol{x})$

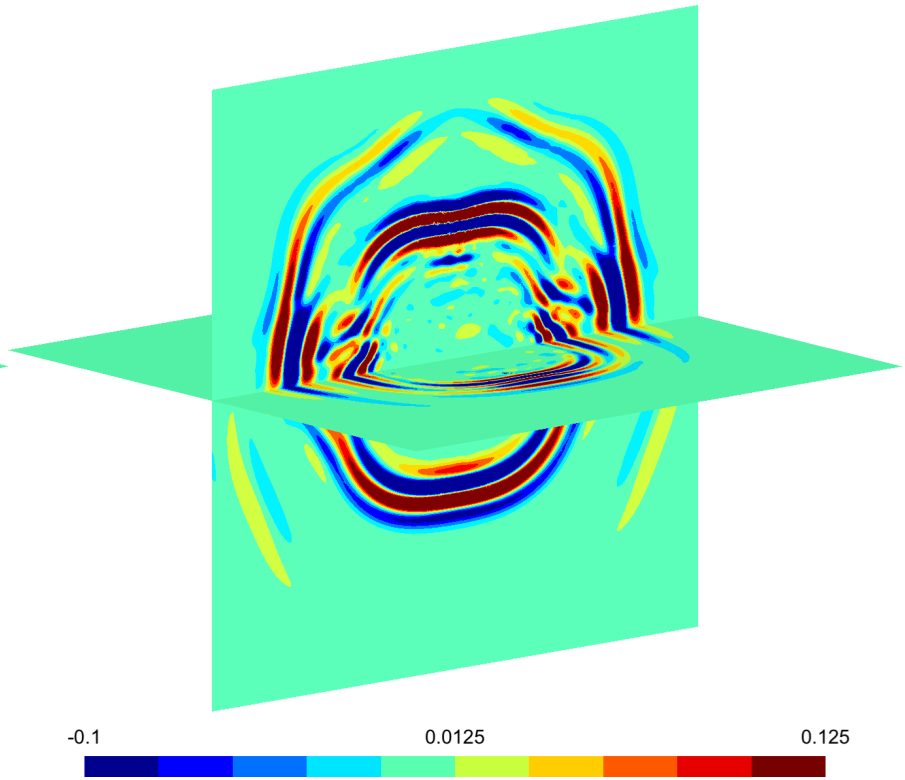

(b) Piecewise constant $\boldsymbol{C}(\boldsymbol{x})$

Figure: $\mathrm{tr}(\boldsymbol{\sigma})$ with $\mu(\boldsymbol{x}) = 1 + H(y) + \frac{1}{2}\cos(3\pi x)\cos(3\pi y)\cos(3\pi z)$, $N = 5$.

Summary and acknowledgements

- **Sparsity** of Bernstein-Bezier DG: efficiency at high orders on GPUs.
- Weight-adjusted DG (WADG): low-storage methods for heterogeneous media and curvilinear meshes.
- Future work:
  - Exploit structure of WADG under Bernstein-Bezier basis.
  - WADG with singular weights.

Thanks to TOTAL E&P Research and Technology USA for their support of this work.

Chan 2017. Weight-adjusted DG methods: matrix-valued weights and elastic wave prop. in heterogeneous media (arXiv).

Chan, et al. 2016. Weight-adjusted DG methods: wave propagation in heterogeneous media (arXiv).

Chan, et al. 2016. Weight-adjusted DG methods: curvilinear meshes (arXiv).

Chan, Warburton 2015. GPU-accelerated Bernstein-Bezier DG methods for wave problems (SISC).

Additional slides

Roofline model: estimating computational efficiency

- Arithmetic intensity: floating-point operations per byte of data.
- Computational efficiency: ratio of observed/achievable performance.

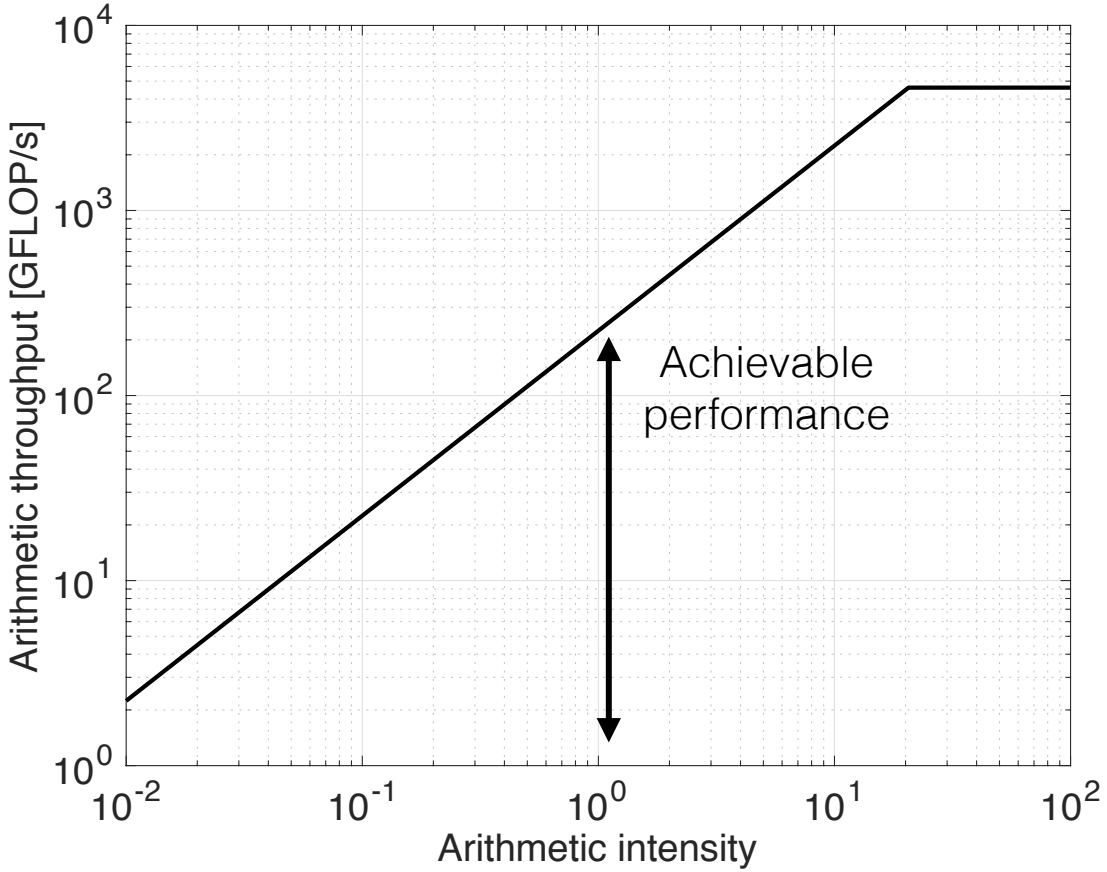

Williams, Waterman, Patterson 2009. Roofline: an insightful visual performance model for multicore architectures.

Roofline model: estimating computational efficiency

- Arithmetic intensity: floating-point operations per byte of data.
- Computational efficiency: ratio of observed/achievable performance.

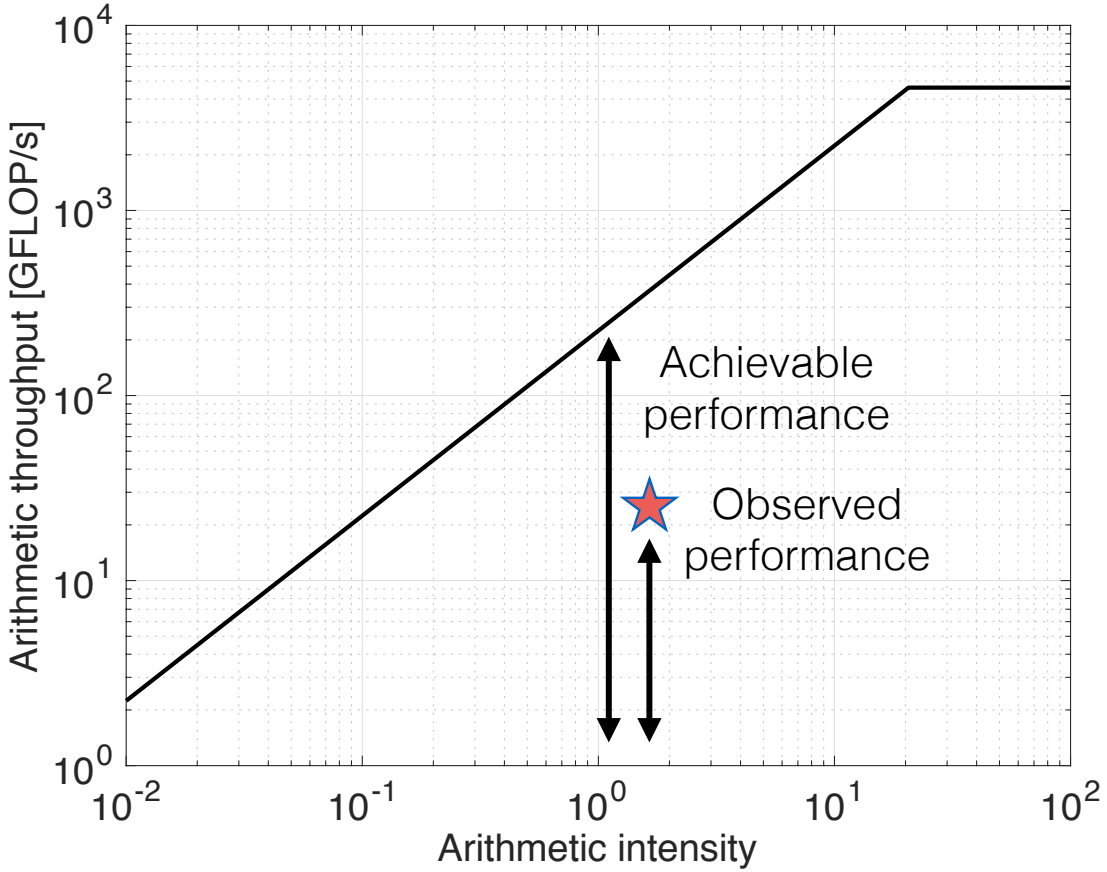

Williams, Waterman, Patterson 2009. Roofline: an insightful visual performance model for multicore architectures.

Roofline model: estimating computational efficiency

- Arithmetic intensity: floating-point operations per byte of data.
- Computational efficiency: ratio of observed/achievable performance.

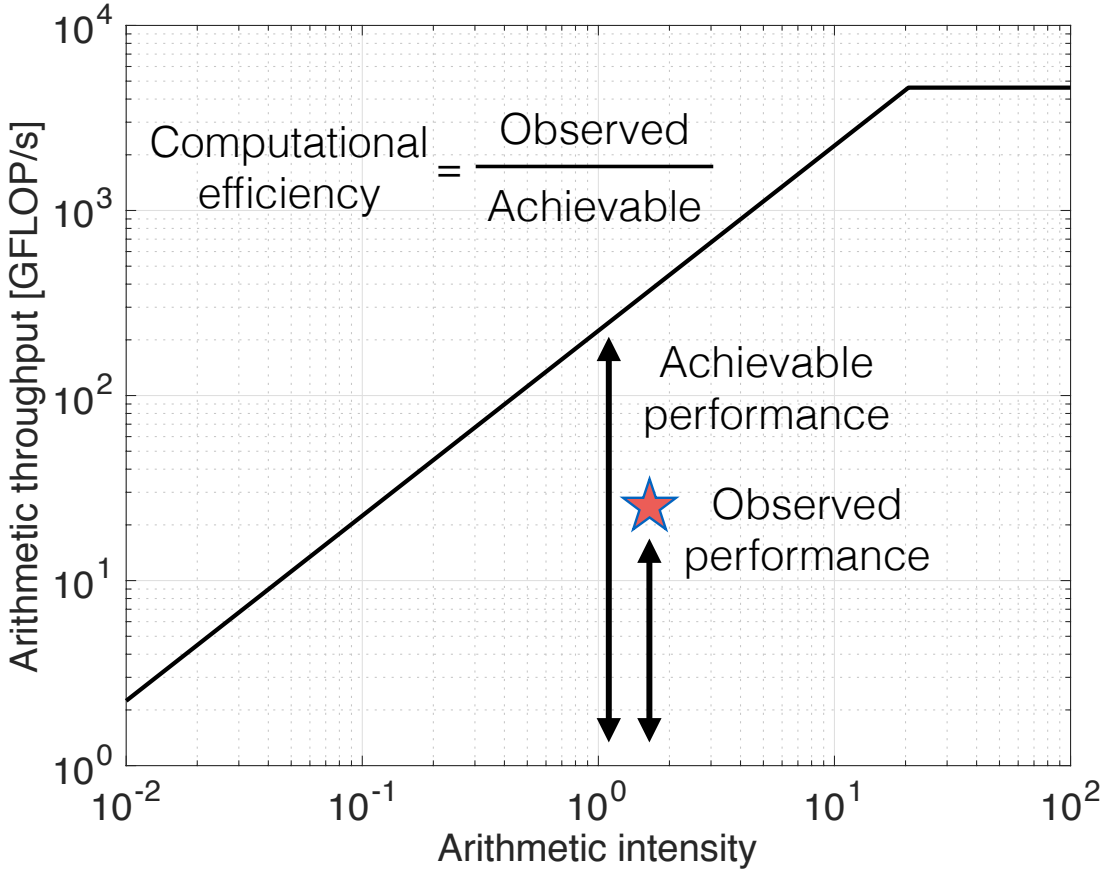

Williams, Waterman, Patterson 2009. Roofline: an insightful visual performance model for multicore architectures.

Performance comparisons of Bernstein-Bezier DG

Bernstein-Bezier DG: standard implementation, sparse matrices.

$$\underbrace{\frac{\mathrm{d}\boldsymbol{u}}{\mathrm{d}t}}_{\text{Update kernel}} = \underbrace{\mathbf{D}_x\mathbf{u}}_{\text{Volume kernel}} + \underbrace{\sum_{\text{faces}} \mathbf{L}_f\,(\text{flux})}_{\text{Surface kernel}}, \quad \mathbf{L}_f = \mathbf{M}^{-1}\mathbf{M}_f.$$

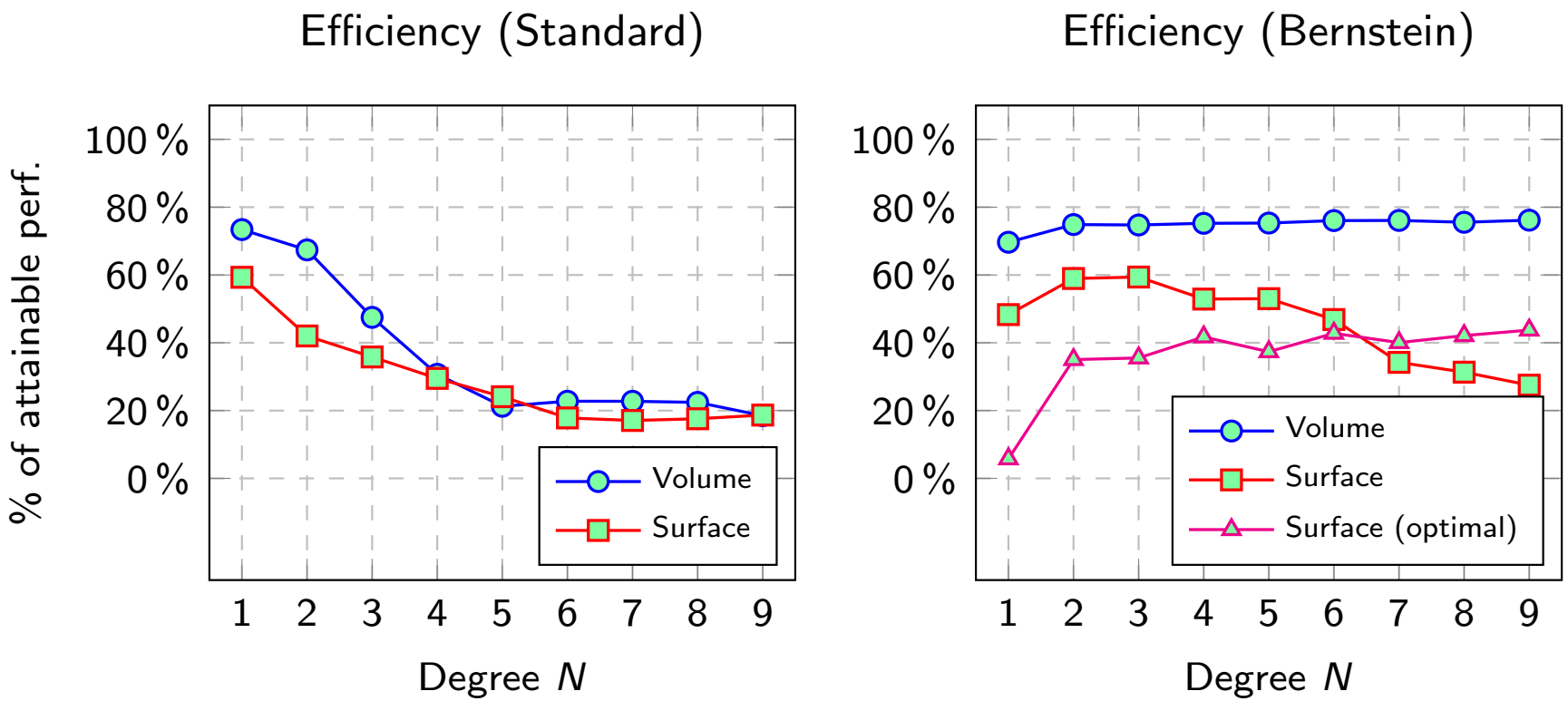

Bernstein-Bezier compared to CUBLAS

Bernstein-Bezier DG achieves $\approx 4\times$ speedup at low-moderate orders, and $1.5 - 2\times$ speedup at high orders.

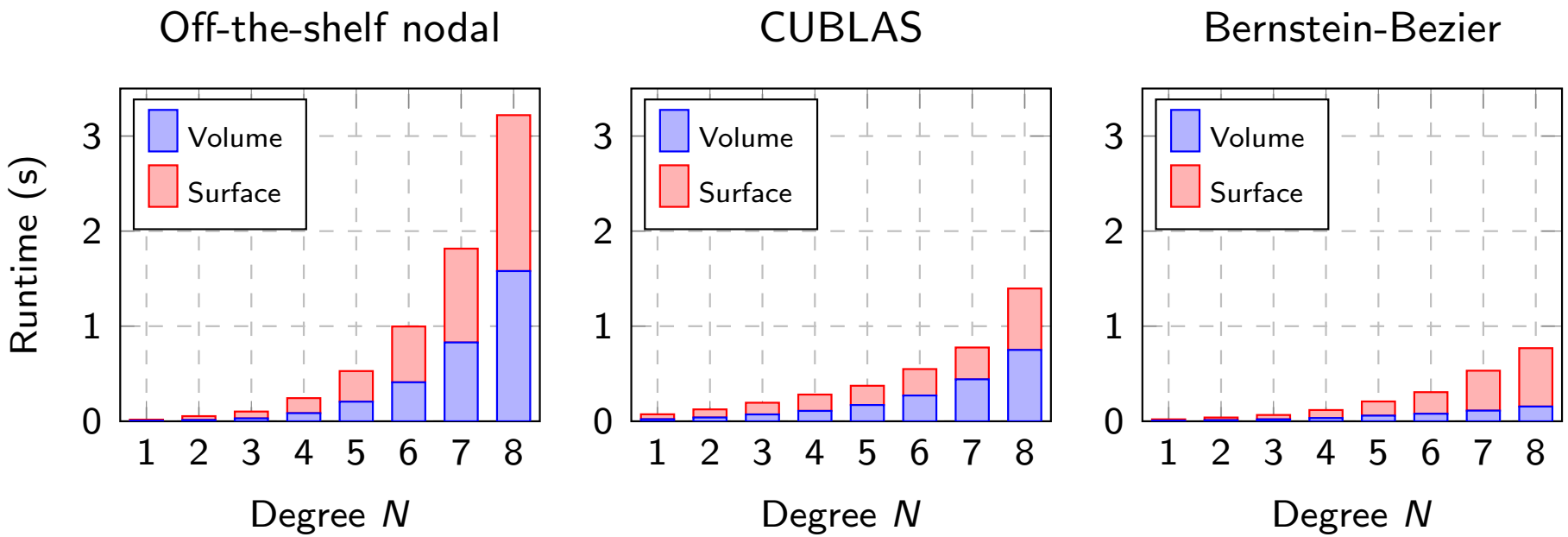

$$\underbrace{\frac{\mathrm{d}\mathbf{u}}{\mathrm{d}t}}_{\text{Update kernel}} = \underbrace{\mathbf{D}_x\mathbf{u}}_{\text{Volume kernel}} + \underbrace{\sum_{\text{faces}} \mathbf{L}_f\,(\text{flux})}_{\text{Surface kernel}}, \quad \mathbf{L}_f = \mathbf{M}^{-1}\mathbf{M}_f.$$

Bernstein-Bezier compared to CUBLAS

Bernstein-Bezier DG achieves $\approx 4\times$ speedup at low-moderate orders, and $1.5 - 2\times$ speedup at high orders.

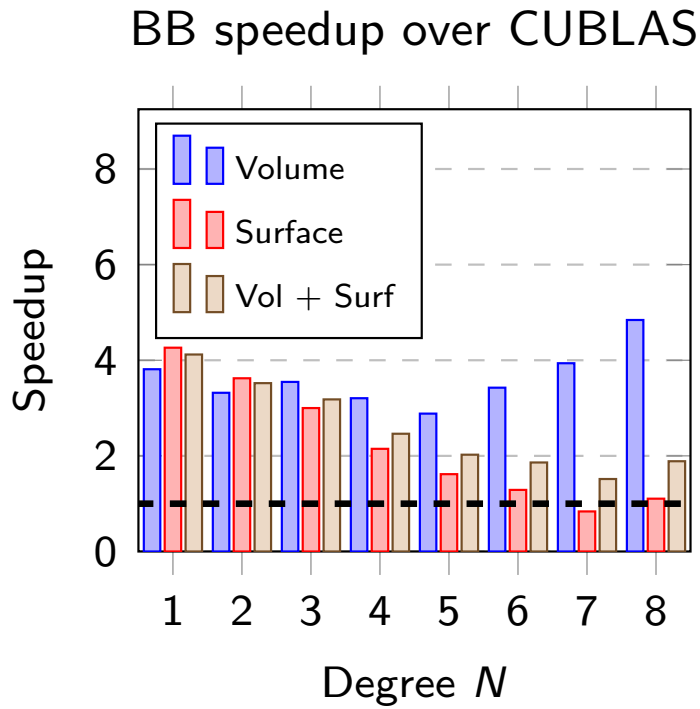

$$\underbrace{\frac{\mathrm{d}\mathbf{u}}{\mathrm{d}t}}_{\text{Update kernel}} = \underbrace{\mathbf{D}_x\mathbf{u}}_{\text{Volume kernel}} + \underbrace{\sum_{\text{faces}} \mathbf{L}_f\,(\text{flux})}_{\text{Surface kernel}}, \quad \mathbf{L}_f = \mathbf{M}^{-1}\mathbf{M}_f.$$

Performance comparisons of Bernstein-Bezier DG

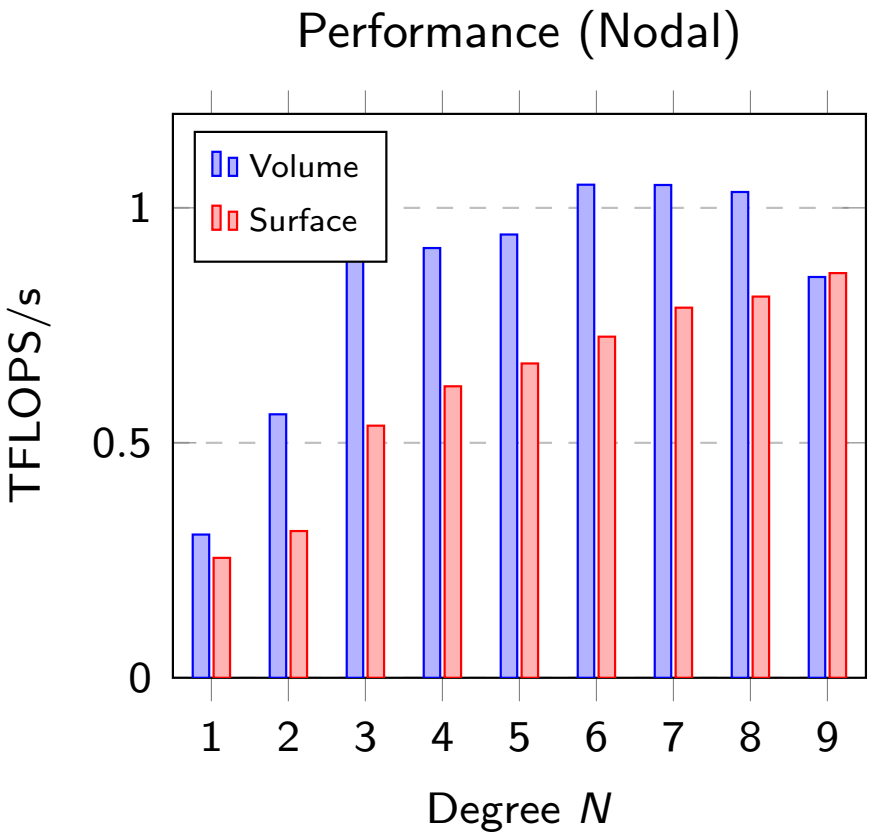

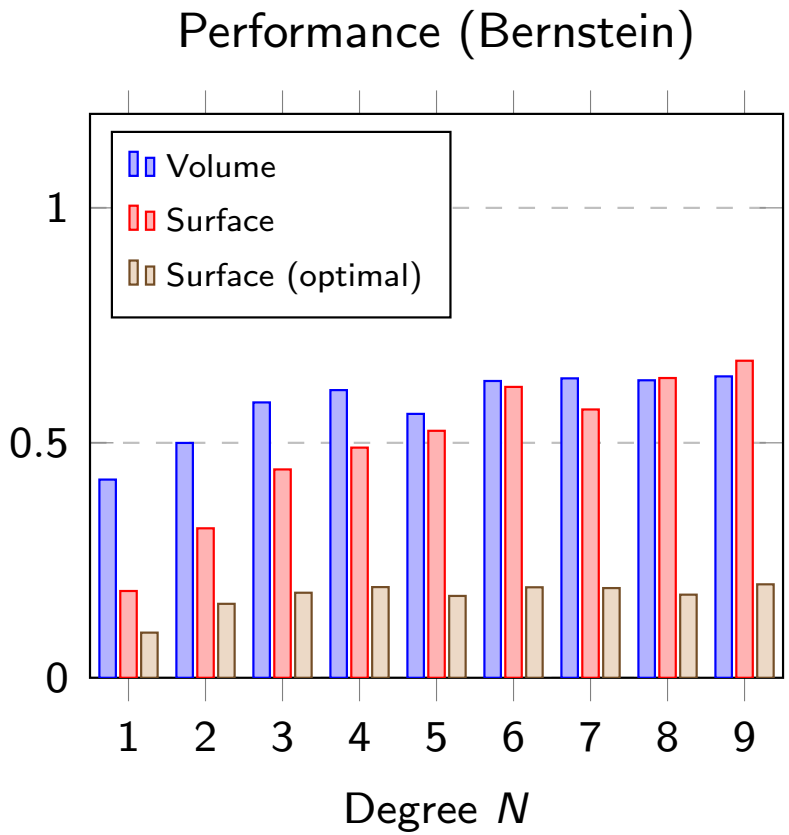

Performance comparisons of Bernstein-Bezier DG

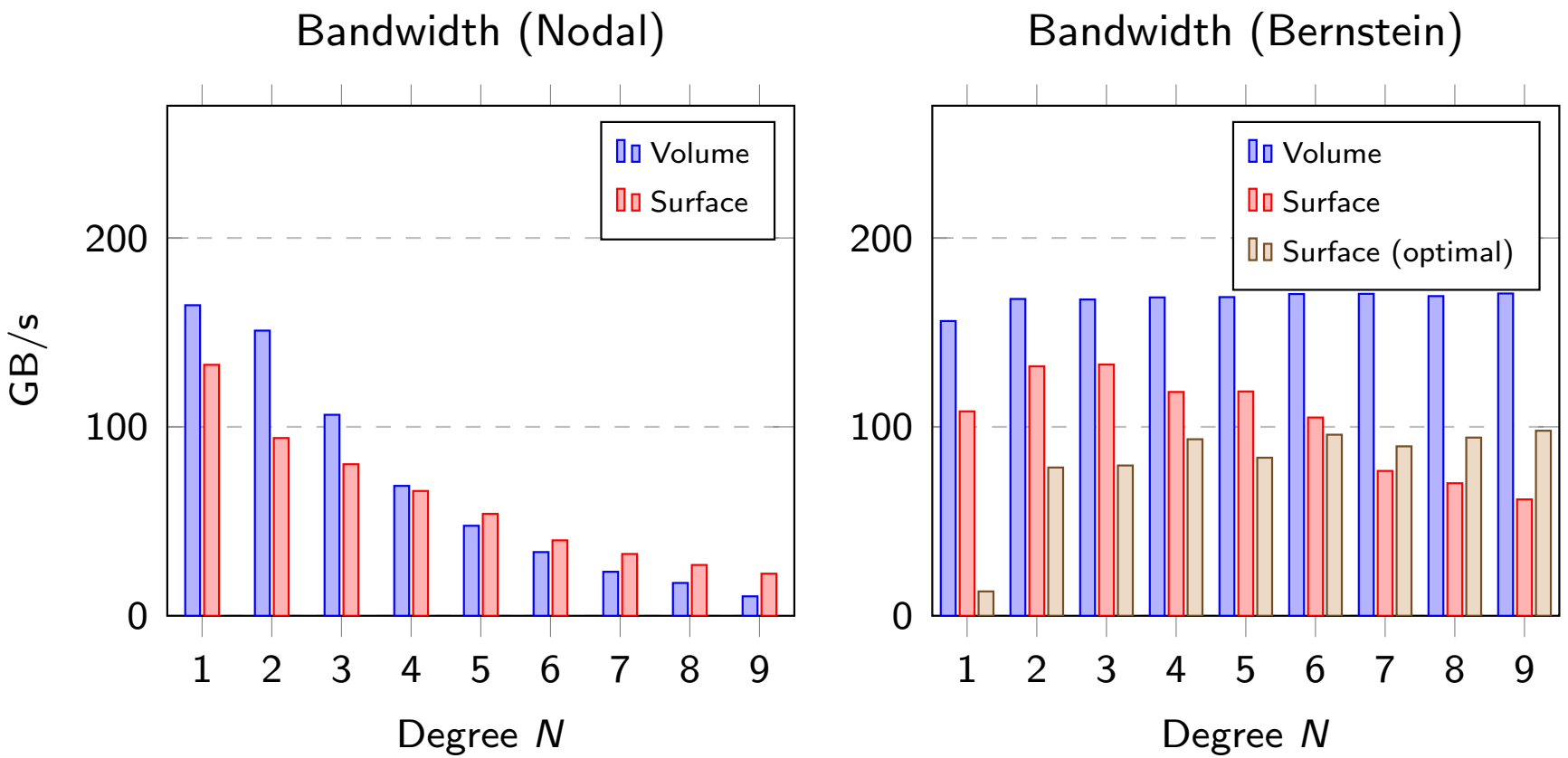

Preliminary comparisons: BBDG, SEM-DG on GPUs

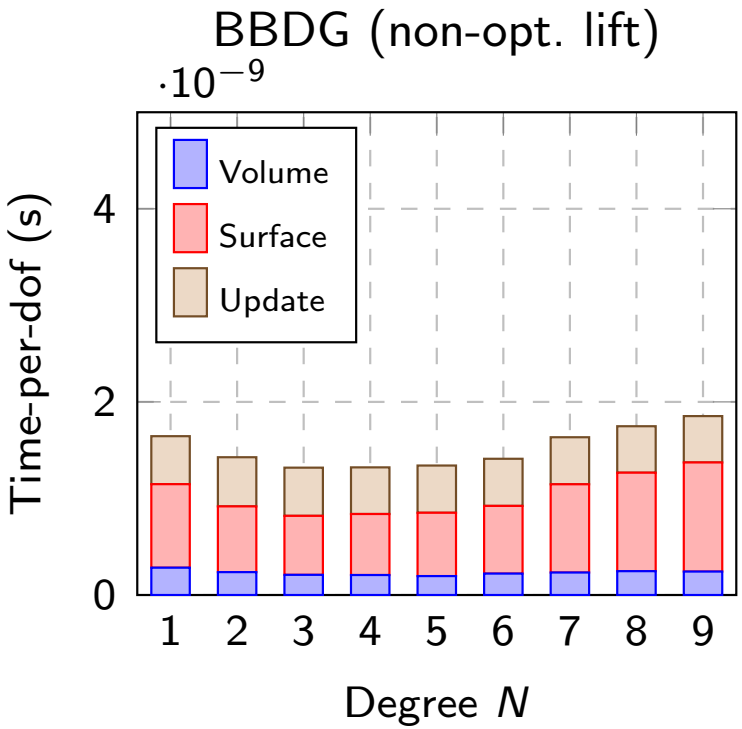

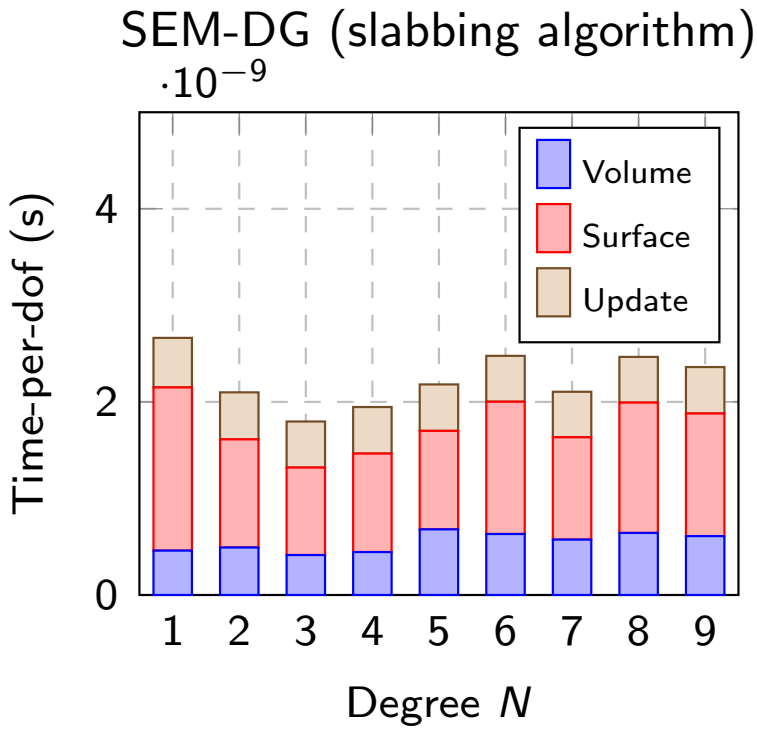

- BBDG 1-1.75$\times$ faster per dof than SEM-DG for $N \leq 10$.
- Unstructured hex meshes: $9(N+1)^3$ geometric factors per element.
- Disclaimer: hexes are more accurate, need time-to-error studies!

Abdi, Wilcox, Warburton, Giraldo 2016. A GPU Accel. Cont. and Disc. Galerkin Non-hydrostatic Atmospheric Model

Preliminary comparisons: BBDG, SEM-DG on GPUs

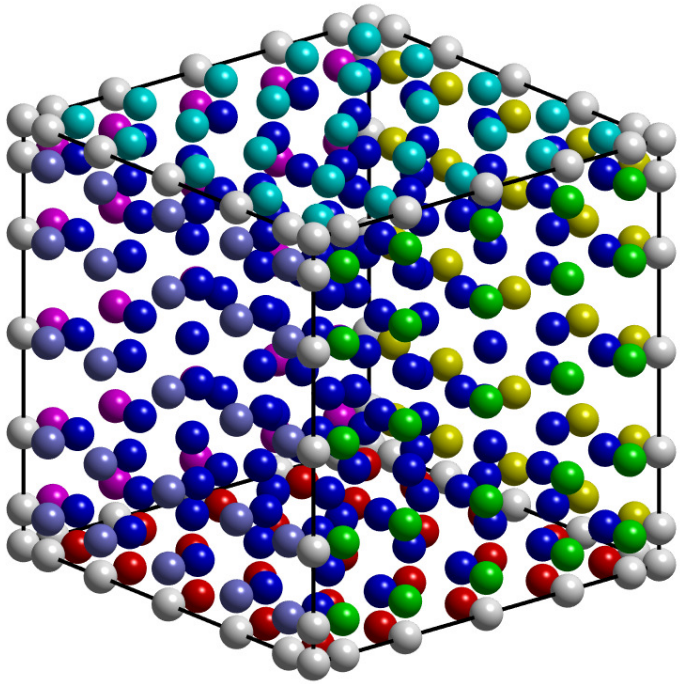

- BBDG 1-1.75$\times$ faster per dof than SEM-DG for $N \leq 10$.
- Unstructured hex meshes: $9(N+1)^3$ geometric factors per element.
- Disclaimer: hexes are more accurate, need time-to-error studies!

Abdi, Wilcox, Warburton, Giraldo 2016. A GPU Accel. Cont. and Disc. Galerkin Non-hydrostatic Atmospheric Model

Effect of conservation on shock speeds

- Weighted Burgers' equation, $w(x)$ curves characteristic lines.

$$w(x)\frac{\partial u}{\partial t} + \frac{1}{2}\frac{\partial u^2}{\partial x} = 0.$$

- WADG yields high order convergence, correct shock speed for both $w(x)$ smooth, discontinuous (within an element).

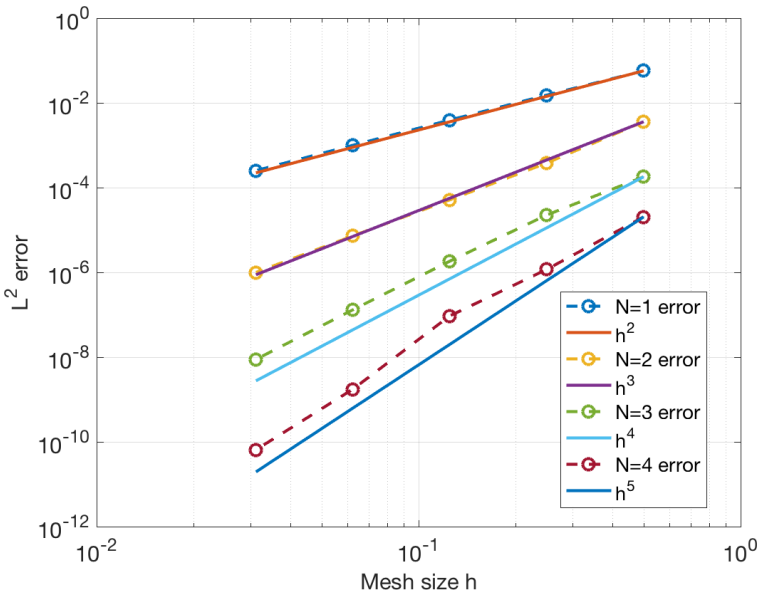

(n) Smooth solution

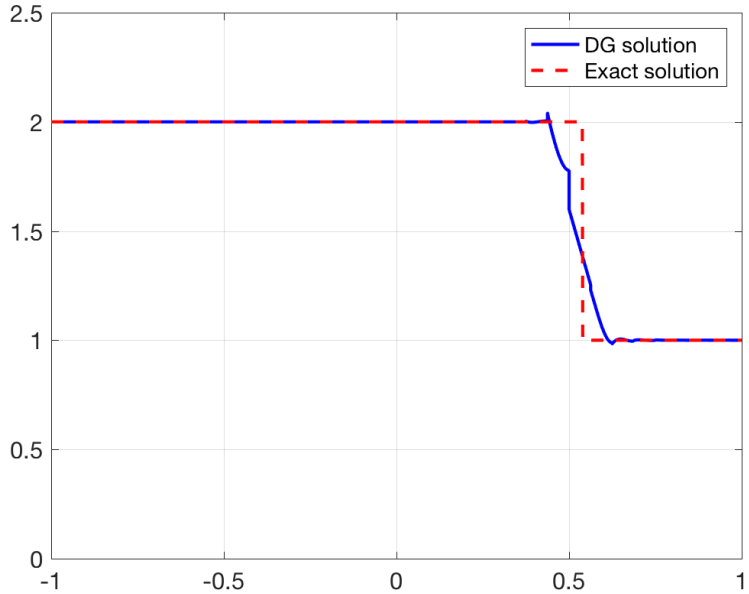

(o) Shock solution

Effect of conservation on shock speeds

- Weighted Burgers' equation, $w(x)$ curves characteristic lines.

$$w(x)\frac{\partial u}{\partial t} + \frac{1}{2}\frac{\partial u^2}{\partial x} = 0.$$

- WADG yields high order convergence, correct shock speed for both $w(x)$ smooth, discontinuous (within an element).

Best guess: where and what is locally conserved matters;
non-conservation of *nonlinear flux* results in incorrect shock speeds.